Supplementary Materials

An eco- and user-friendly textile integrating radiative heating and cooling for large-temperature-variation personal thermal management

Jiankang Zhang[a,b], Huilin Dong[a], Yian Yu[a], Mengyao Cao[a], Cuihuan Li[a], Xiaoying Shen[a], Junying Li[a], Yanglei Xu[a], Sheng Chen[a,b,*], Feng Xu[a,b,*]

[a]State Key Laboratory of Efficient Production of Forest Resources, Beijing Forestry University, Beijing 100083, China

[b]Beijing Key Laboratory of Lignocellulosic Chemistry, Beijing Forestry University, Beijing 100083, China

[*]Corresponding authors

E-mail addresses: shengchen@bjfu.edu.cn (S. Chen); xfx315@bjfu.edu.cn (F. Xu)

This PDF file includes:

Supplementary Notes 1 to 8

Supplementary Figs. S1 to S40

Tables S1 to S2

Supplementary Movies 1 to 2

References

Supplementary Note 1. Heat transfer model analysis

We use a one-dimensional steady-state heat transfer model analysis to determine the impact of i-textile's optical properties on the required set-point of environment temperature for maintaining thermal comfort in indoor and outdoor environments[1]. This model includes heat radiation, conduction, convection, absorption, and reflection of sunlight in the outdoor environment to simulate human body heat dissipation and sunlight absorption from a clothed human body to the ambient environment (Supplementary Fig. 2). The criterion for thermal comfort is set as the equality of the total heat dissipation rate with the total heat generation rate. Based on energy balance, the heat dissipation flux should equal the metabolic heat generation flux at every position in the system. The net radiation equations with non-radiative components of heat transfer are as follows:

At the skin surface

$$q_{gen} + \rho_i\, q_{rad,s} + \tau_t\, q_{rad,e} + q_{rad,i} - q_{rad,s} - q_{cond,a} = 0$$

At the textile

$$(1 - \tau_t - \rho_i)\, q_{rad,s} + (1 - \tau_t - \rho_0)\, q_{rad,e} + q_{cond,a} - q_{rad,o} - q_{rad,i} - q_{conv} + q_{sun} = 0$$

Within the textile, the temperature profile has the following analytical formulation,

$$T_o = t_t(2k_t)\,(q_{rad,i} + q_{rad,o} - \alpha_i q_{rad,s} - \alpha_o q_{rad,e} - q_{sun}) - k_a t_t(k_t t_a)(T_s - T_i) + T_i$$

Here, q_{gen} is the metabolic heat generation rate per unit area, $q_{rad,s}$ is the radiative heat flux from the skin, $q_{rad,e}$ is the radiative heat flux from the ambient environment, $q_{rad,i}$ is the radiative heat flux from the textile inner surface, $q_{rad,o}$ is the radiative heat flux from the textile outer surface, $q_{cond,a}$ is the conductive heat flux in the air gap between the skin and the textile, q_{conv} is the convective heat flux from the textile to the ambient environment. q_{sun} is the heat generation rate due to solar absorption, which is zero in indoor and outdoor environments without sunlight.

According to Fourier's law, Newton's law of cooling and the Stefan-Boltzmann law, the conductive, convective and radiative heat flux terms can be expressed as[2],

$$q_{rad,s} = \varepsilon_s \, \sigma \, T_s^4$$

$$q_{rad,e} = \varepsilon_e \, \sigma \, T_e^4 \quad \text{(indoor)}$$

$$q_{rad,e} = \int_0^{\frac{\pi}{2}} \pi \sin(2\theta) \mathrm{d}\theta \int_0^{\infty} (I_s(\lambda, T_e) \, \varepsilon_o \, (1 - \mathrm{t}(\lambda)^{1/\cos(\theta)}) \mathrm{d}\lambda \quad \text{(outdoor)}$$

$$q_{rad,i} = \varepsilon_i \, \sigma \, T_i^4$$

$$q_{rad,o} = \varepsilon_o \, \sigma \, T_o^4 \quad \text{(indoor)}$$

$$q_{rad,o} = \varepsilon_o \int_0^{\frac{\pi}{2}} \pi \sin(2\theta) d\theta \int_0^{\infty} I_s(\lambda, T_o) \, \mathrm{d}\lambda \quad \text{(outdoor)}$$

$$q_{cond,a} = \left(\frac{k_a}{t_a}\right) \cdot (T_S - T_i)$$

$$q_{conv} = h \cdot (T_o - T_e)$$

$$q_{sun} = \int_0^{\infty} \alpha \, (\lambda, \theta_{sun}) \, I_{AM1.5}(\lambda) d\lambda \quad \text{(outdoor, sunlight)}$$

I_s (λ, T_e) signifies the intensity of spectral irradiation emitted by a blackbody at temperature T_e. The expression $(1-t(\lambda)^{1/cos\theta})$ represents the atmospheric emissivity, where $t(\lambda)$ stands for the spectral transmittance of the atmosphere in the zenith direction. α (λ, θ_{sun}) represents the absorbance in the sunlight wavelength λ, θ_{sun} is the angle between the sample and sunlight, and $I_{AM1.5}(\lambda)$ denotes the sunlight irradiance at wavelength λ. The remaining input parameters are listed in Supplementary Table 1 below. Note that the textile thermal conductivity k_t is an effective value of the textile as a whole, considering the existence of air gaps in the textile.

Based on the one-dimensional steady-state heat transfer model, we assume that the environment temperature is 25 °C and the skin temperature is maintained at 33.5 °C. Based on the above equations and known parameters, the three unknowns, q_{gen}, T_i and T_o, can be solved with the input of ε_i and ε_o values ranging from 0 to 1. The resulting q_{gen} corresponds to the required heat gain rate for the i-textile to maintain thermal comfort at a constant skin temperature (T_s = 33.5 °C) and environment temperature (T_e = 25 °C) (Fig. 1d). When q_{sun} is 500 W/m^2, the relationship between q_{gen} and solar absorptivity α can be derived by fixing the emissivity to 0 and 1 (Fig. 1e).

Based on the above equations and known parameters, the three unknowns, T_e, T_i and T_o, can be solved with the input of ε_i and ε_o values ranging from 0 to 1. The resulting T_e

corresponds to the required set-point for the i-textile to maintain thermal comfort at a constant skin temperature ($T_s = 33.5$ °C) and heat generation rate (75 W m^{-2}) in indoor, outdoor without sunlight (dark days) and outdoor with sunlight (daytime) environments. Note: Different formulas are required for indoor and outdoor environments.

Supplementary Note 2. Quantitative contribution of factors for human body heat loss

Human body heat maintenance/loss is generally a very complicated processing[3]. The human body dissipates heat through four routes: radiation, conduction, convection, and evaporation. Human body dissipates heat mainly through radiation when the skin temperature is below 33.5 ℃ and the environmental temperature is below 30 ℃, representing a typical indoor environment. To be more specific, heat loss through radiation accounts for ~ 60%, while evaporation and convection contribute to 22% and 15% of heat dissipation respectively when the indoor temperature is around 25 ℃ (Supplementary Fig. 3). Therefore, to facilitate heating and cooling from the human body in such indoor environment, controlling thermal radiation is the most important and effective.

Supplementary Note 3. Finite-Difference-Time-Domain Simulations

The optical simulation is based on Mie theory and Chandrasekhar radiative transfer theory. To theoretically investigate the influence of CA nanofiber diameter and MXene nanosheet size on scattering properties, Finite-Difference-Time-Domain (FDTD) simulations are carried out[4, 5]. A total field scattering field (TFSF) source is used, and the perfect matching layer (PML) is utilized as the absorption boundary condition. The FDTD domain is set to accommodate different diameter nanofibers or sizes of MXene nanosheets. The simulated diameters of the CA nanofibers range from 50-1800 nm and the size of MXene nanosheets range from 200-2000 nm. The source is across the main solar region (0.3-2.0 μm). The appropriate mesh size is determined to achieve a good trade-off between computer memory requirements and simulation time. The scattering cross-sections of the CA nanofibers with different diameters or the MXene nanosheets with different sizes can be calculated by the cross-section analysis groups. The scattering efficiencies are calculated by dividing the scattering cross-sections by the geometrical cross-sections.

Supplementary Note 4. Average mid-infrared spectral emissivity (absorptivity) analysis.

The average mid-infrared spectral emissivity at 7-14 μm of the i-textile is calculated according to the following equations[6]:

$$\varepsilon(T) = \frac{\int_{7\mu m}^{14\mu m} \varepsilon(\lambda)\, L(\lambda) d\lambda}{\int_{7\mu m}^{14\mu m} L(\lambda) d\lambda}$$

$$L(\lambda) = \frac{C_{IL}}{\lambda^5 \left[\exp\left(\frac{C_2}{\lambda T}\right) - 1\right]}$$

where, ε(λ) is the spectral emissivity measured based on the thermal radiation relation, i.e., $\varepsilon = 1 - \rho - \tau$ (ε, ρ and τ are emissivity, reflectivity and transmissivity, respectively). The reflectivity (ρ) and transmissivity (τ) are obtained from an FTIR spectrometer (Nicolet iS50, Thermo Fisher) accompanied by an infrared integrating sphere. L(λ) is the spectral radiance emitted from the blackbody, where C_{IL} is the first radiation constant for spectral radiance, $C_{IL} = 2hc^2 = 1.191 \times 10^8$ (W μm^4 m^{-2} sr). C_2 is the second radiation constant, $C_2 = hc/K_B = 1.439 \times 10^4$ (μm K). K_B is the Boltzmann constant, h is the Planck constant, and c is the speed of light in a vacuum. T is the room temperature (25 °C) when measuring the spectral emissivity.

The average spectral absorptivity (α) at 0.2-2.5 μm of i-textiles is the irradiance-weighted average of its spectral absorptivity and is calculated according to the following equation[7]:

$$\alpha(T) = \frac{\int_{0.2\mu m}^{2.5\mu m} \alpha(\lambda)\, i(\lambda) d\lambda}{\int_{0.2\mu m}^{2.5\mu m} i(\lambda) d\lambda}$$

where $\alpha(\lambda)$ is spectral absorptivity obtained based on the relation, i.e., $\alpha = 1 - \rho - \tau$ (α, ρ and τ are spectral absorptivity, reflectivity and transmissivity, respectively). The spectral reflectivity (ρ) and transmissivity (τ) are obtained using a UV-VIS-NIR spectrometer (UV3600 plus, Shimadzu) accompanied by an infrared integrating sphere. $i(\lambda)$ is the solar spectral irradiance (W m^{-2} nm^{-1}) obtained from ASTM standard G173-03.

Supplementary Note 5. Indoor thermal management measurements

The human skin was effectively simulated using a silicone rubber flexible heater that was covered with 3M insulating tape. A ribbon-type hot-junction thermocouple (0.3 mm in diameter, K-type) was placed in direct contact with the top surface of the simulated skin to measure the skin temperature (Supplementary Fig. 27b). In order to isolate the heat generated by the simulated skin and prevent any unwanted heat transfer, a guard heater and insulating foam were positioned beneath the simulated skin heater. The temperature of the guard heater was consistently set the same as the skin heater. The entire device was enclosed within a chamber, and the ambient temperature inside the chamber could be controlled. The power density of the simulated skin heater was set at a constant value of 75 W m^{-2}, resulting in a skin temperature of 33.5 °C at an ambient temperature of 25 °C. When various textiles were placed over the skin, the steady-state ambient temperature required to sustain the skin temperature at 33.5 ± 0.5 °C was measured. The heating power of the skin heater continued to be maintained at 75 W m^{-2}, while the ambient temperature was kept at 25 °C. The temperatures of the simulated skin covered with different textiles were carefully recorded. Additionally, temperature measurements were conducted on simulated skin covered with cotton and i-textile by adjusting the chamber ambient temperature to vary across a large-temperature range of 14.7-27.3 °C. The cooling surface of the i-textile was faced outwards for higher ambient temperatures and the heating surface was faced outwards for lower temperatures. Thermal management tests involving a large-temperature-difference were conducted by covering the i-textile onto the surface of actual human skin. To assess the heating performance of the i-textile, demonstrations were carried out during specific time intervals, namely 8-9 AM and 5-6 PM. Subsequently, the textile was flipped over, and the cooling performance was showcased at 12-1 PM. The temperature between the i-textile and actual human skin was tested using thermocouples.

Supplementary Note 6. Outdoor thermal management measurements

For the outdoor thermal test, the i-textile was placed in a foam container elevated to a height of 0.8 m above the ground to prevent heat conduction from the ground and ensure negligible heat loss (Fig. 4a). This thermal measurement apparatus was covered with a layer of aluminum film (radiation shield) to reflect the solar power and thermal radiation from the surroundings. The i-textile was attached to a copper plate for flatness and placed in its container. The heating surface of the i-textile faced the sky during low-temperature time intervals, namely 7-10 AM and 4-7 PM, while the cooling surface faced during the high-temperature time period between 11-3 PM. The ambient temperature and the temperature between the i-textile and the copper plate were recorded using thermocouples. For the skin simulator thermal test, a silicone rubber flexible heater was introduced into the container to simulate the skin spectrum and the body's metabolic heat generation. Apart from this, the rest of the apparatus was the same as the ambient thermal test. The temperature of the skin simulator covered with the i-textile was recorded by a thermocouple, and the operating time of heating and cooling surfaces was consistent with the ambient thermal test. For comparison, thermal measurements were also conducted on cotton textile and bare simulated skin under identical test conditions. Throughout the thermal test process, the apparatus was exposed to direct sunlight and air. To monitor parameters in real-time, such as solar irradiance, wind speed, and relative humidity, a pyranometer (CEL-NP2000) and a digital anemometer (HP-866, HoldPeak) were employed at the experiment site. Demonstrations of the ambient thermal and skin simulator thermal tests of the samples were carried out under clear skies in Haidian, Beijing, China (40° 00′N, 116° 34′E) on May 7, 2023 and May 22, 2023, respectively.

Supplementary Note 7. Additional modeling of energy consumption patterns

The energy-saving potential of the i-textile is estimated using EnergyPlus with reference to large-sized apartment and office buildings (Supplementary Fig. 31)[8, 9]. Thirty cities in seven building climate zones of China are selected as representative cities to investigate the energy-saving performance in different climate zones. For the high-rise multifamily apartment, the building comprises 10 floors with 8 apartments on each floor, except for the ground level, which includes 7 apartments and 1 office area, all having an equivalent apartment area. The floor-to-ceiling height stands at 3.1 m, while the windows measure 1.2 m in height by 0.9 m in width. The external walls are meticulously constructed with steel-frame structures, enriched with stucco, gypsum board, and wall insulation materials, all contributing to bolster thermal performance. For weather resistance, the roof of the building incorporates a composite system, featuring a roof membrane, roof insulation, and metal decking. The foundation comprises unheated slab-on-grade floors, constructed by directly pouring a 20.3 cm thick concrete slab onto the natural terrain. Internal partitions within the building are constructed as uninsulated stud walls, contributing to the overall structural composition of the high-rise apartment.

In the case of the large office building, it includes 12 above-ground floors and an additional basement level. The architectural design of this building integrates a window-to-wall ratio of 40% for the gross above-grade walls, meticulously distributing windows evenly across all four facades. Regarding thermal zoning, each floor is meticulously subdivided into four distinct perimeter zones, along with a central core zone and a specialized closet zone. Notably, the basement floor serves a dedicated purpose as a datacenter zone, encompassing 28% of the entire basement area. The exterior walls are constructed using a combination of pre-cast concrete panels and heavy-weight concrete, fortified with wall insulation materials and gypsum board for enhanced insulation and structural integrity. The roofing system comprises a composite ensemble, consisting of a roof membrane, roof insulation, and metal decking. Internally, partitions take the form of uninsulated stud walls. The office building utilizes individual variable air volume (VAV) systems to condition each floor. Each VAV loop consists of a cooling coil and a heating coil fed by a centralized water-cooled centrifugal chiller, and a gas boiler respectively. Reheat air terminals in each zone provide humidity control for occupancy comfort.

The indoor set-point temperature for conventional cotton textiles needs to be 23.0 °C to maintain a comfortable skin temperature of 33.5 °C. In contrast, the i-textile requires distinct set-points for its heating and cooling surfaces. Consequently, when all residents wear the i-textile, it becomes feasible to reduce the thermostat temperature of buildings during winter and increase it in summer. To quantitatively assess the potential impact of our i-textile on building energy efficiency, we employ EnergyPlus to simulate the prospective energy savings in both apartment and office buildings under this adjusted temperature regimen, assuming that every resident is wearing the i-textile.

Supplementary Note 8. DFT calculation

The density functional theory (DFT) calculations are carried out with the VASP code[10, 11]. The Perdew-Burke-Ernzerhof (PBE) functional within the generalized gradient approximation (GGA) is used to process the exchange-correlation, while the projector augmented-wave pseudopotential (PAW) is applied with a kinetic energy cut-off of 500 eV, which is utilized to describe the expansion of the electronic eigenfunctions. The vacuum thickness is set to be 25 Å to minimize interlayer interactions. The Brillouin-zone integration is sampled by a Γ-centered 5 × 5 × 1 Monkhorst-Pack k-point. All atomic positions are fully relaxed until energy and force reach a tolerance of 1×10^{-5} eV and 0.03 eV/Å, respectively. The dispersion corrected DFT-D method is employed to consider the long-range interactions. The binding energies of CA molecular chains and MXene nanosheets, MXene nanosheets and MXene nanosheets with/without the presence of Ca^{2+} ion have been performed via DFT calculations.

Taking CA molecular chains and MXene nanosheets for example, the binding energy can be calculated using the following equation:

$$\Delta E_{bind\ energy} = E_{CA\text{-}MXene} - (E_{CA} + E_{MXene})$$

where $E_{CA\text{-}MXene}$ is the total energy for CA molecular chains and MXene nanosheets, and E_{CA} and E_{MXene} are the binding energies of isolated CA molecular chains and MXene nanosheets, respectively.

The differential charge density of the CA-MXene system with Ca^{2+} ion is defined as:

$$\Delta\rho = \rho_{total} - \rho_{CA} - \rho_{MXene} - \rho_{ion}$$

where ρ_{total}, ρ_{CA}, ρ_{MXene}, ρ_{ion} are the total charge density of the structure, the charge density of CA, MXene, and ions, respectively.

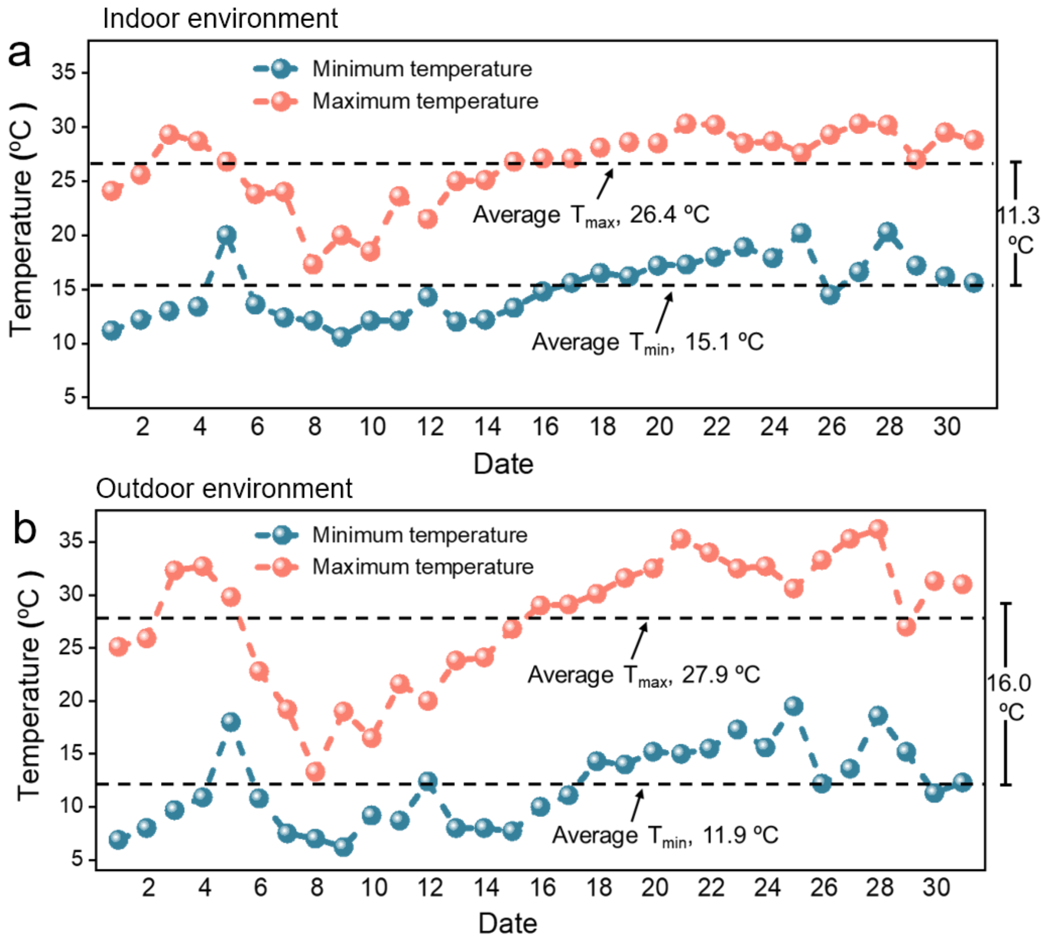

Supplementary Fig. 1. a Indoor and **b** outdoor environments temperature changes in May 2022 in Haidian, Beijing, China.

In the indoor environment, the average maximum temperature is 26.4 ℃ and the minimum is 15.1 ℃, with an average temperature difference of up to 11.3 ℃ (Supplementary Fig. 1a). In the outdoor environment, the average maximum temperature is 27.9 ℃ and the minimum is 11.9 ℃, with a substantial average temperature difference of up to 16.0 ℃ in Haidian, Beijing, China, in May (Supplementary Fig. 1b).

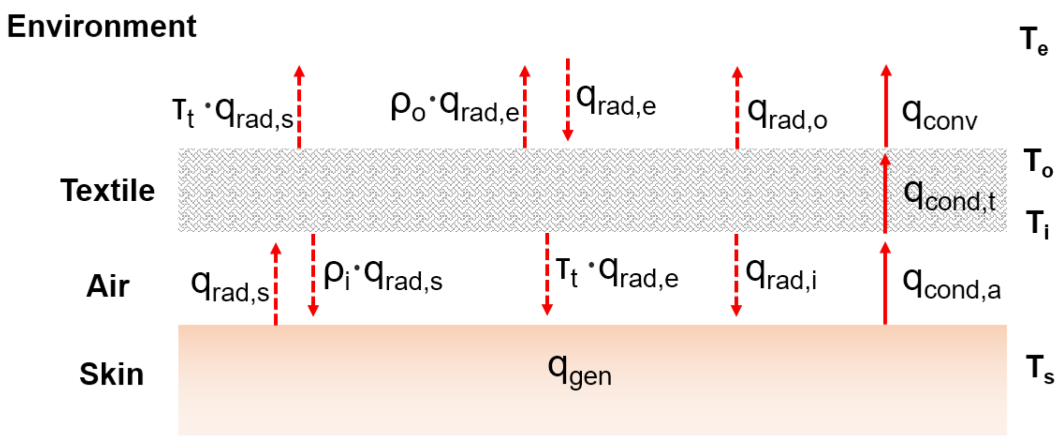

Supplementary Fig. 2. Schematic for one-dimensional steady-state heat transfer model. Schematic illustrating the heat transfer model of a clothed human body.

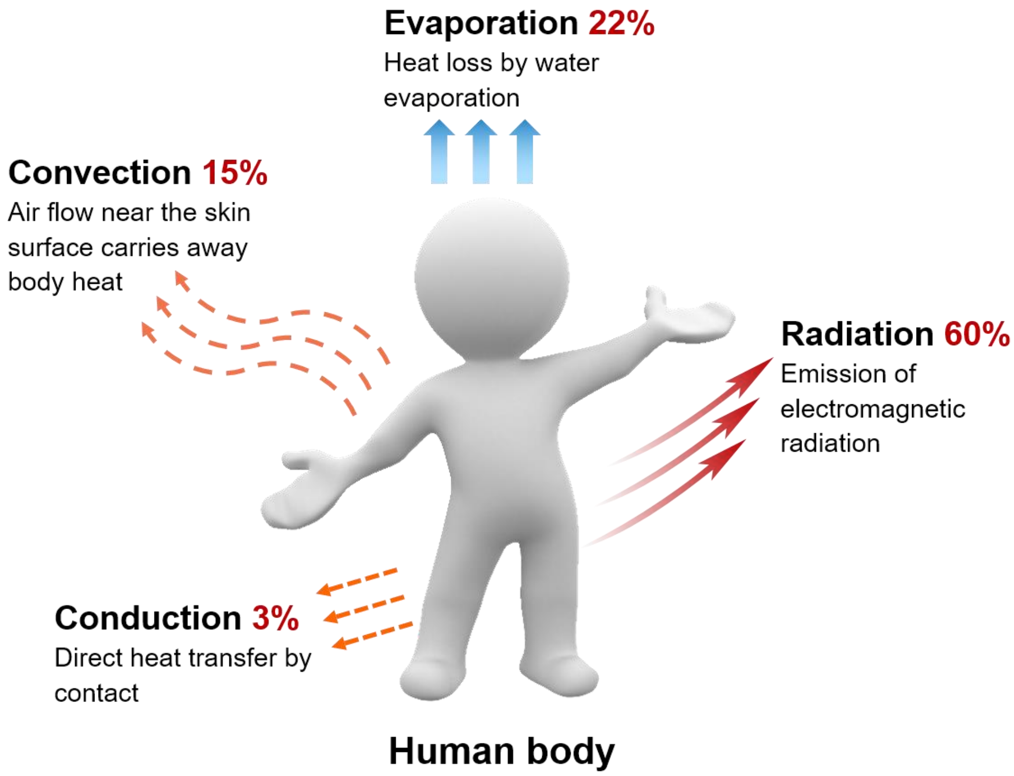

Supplementary Fig. 3. Schematic for human body heat loss distribution.

In the indoor environment, radiative heat transfer is the primary heat dissipation pathway for the human body, which accounts for ~ 60% of the total heat transfer from a human body. Regulating the thermal radiation emissivity can realize PTM[12].

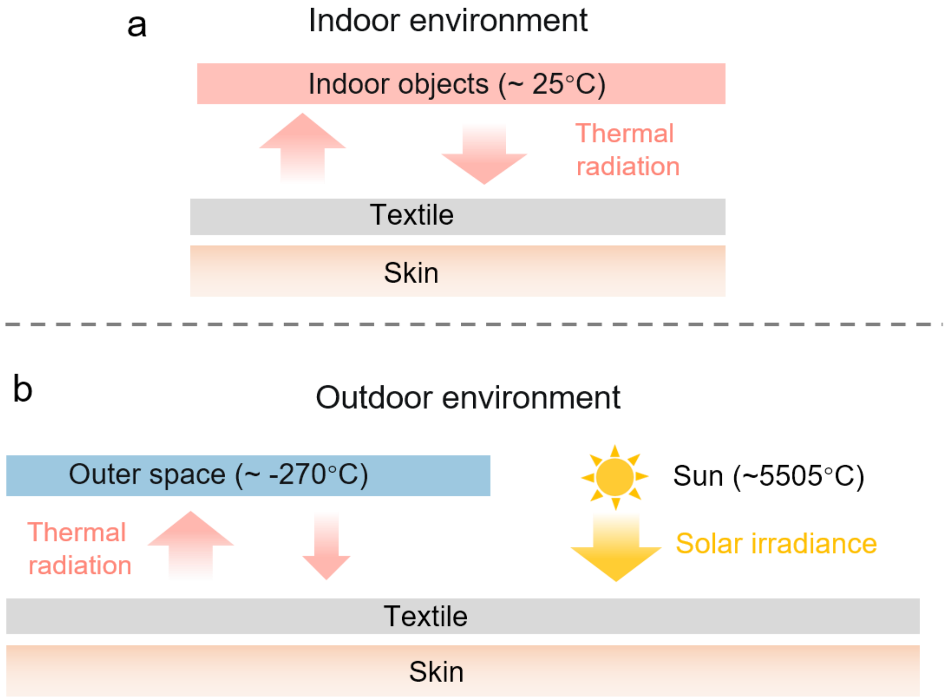

Supplementary Fig. 4. Heat inflow and outflow due to thermal radiation and solar irradiance for PTM in **a** indoor and **b** outdoor environments.

In the indoor environment, the primary avenue for dissipating body heat is through thermal radiation (Supplementary Fig. 4a), accounting for ~ 60% of the total heat loss. The regulation of thermal radiation emissivity on the outside surface of textiles offers a means of achieving PTM. By enhancing the emissivity of the textile's outside surface, the cooling of the human body can be facilitated, while conversely, this approach can also serve heating purposes. To realize eco-friendly PTM in the outdoor environment, two significant challenges demand attention (Supplementary Fig. 4b). Firstly, the presence of the outdoor atmospheric window allows a substantial portion of the body's thermal emissions to escape into the cold outer space (~ -270°C), resulting in much higher radiative loss for personal heating compared to the indoor environment. Secondly, the prevalent outdoor solar irradiation (~1000 W m^{-2} for 1 sun, AM1.5) leads to extra heat load, making it difficult to realize personal cooling. Hence, synergistic modulation of thermal emissivity and solar reflectivity is required to achieve PTM in the outdoor environment[2].

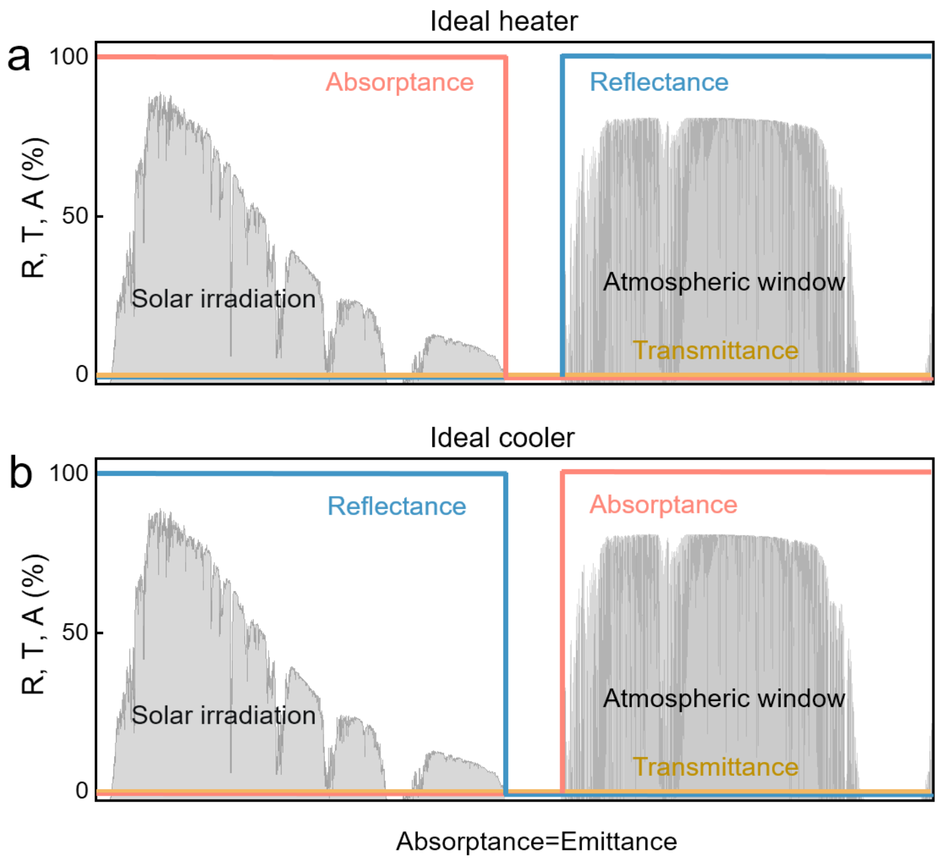

Supplementary Fig. 5. Spectral characterization of ideal radiative **a** heating and **b** cooling materials in solar irradiation and the atmospheric window. R, T, and A represent reflectance, transmittance, and absorptance, respectively.

In the outdoor environment, for an ideal radiative heater, the materials should have high absorptivity in the solar irradiation and low emissivity in the atmospheric window band, determined by the solar spectrum and blackbody radiation law (Supplementary Fig. 5a). Conversely, for an ideal radiative cooler, especially in daytime sub-ambient radiative cooling, the materials are expected to efficiently reflect solar irradiation and also have strong mid-infrared emission in the specific wavelength range of the transparent atmospheric window (Supplementary Fig. 5b)[13].

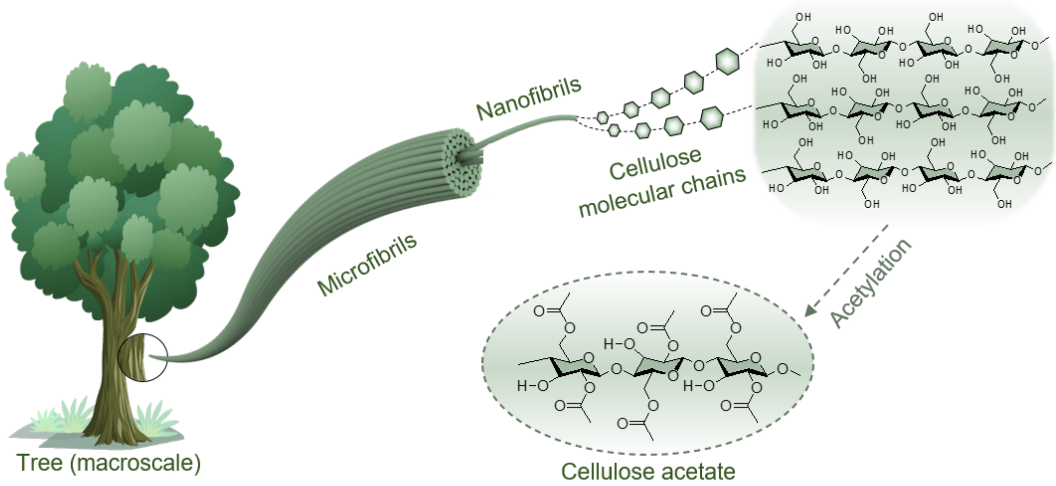

Supplementary Fig. 6. Schemes of the wood's hierarchical structure and the source of CA.

Wood, the fibrous tissue found in stems and roots of trees, is a natural composite consisting of numerous cells[14]. Cellulose microfibril bundles are the main constituents of the wood cell wall, accounting for 40-50%. The cellulose microfibril bundle can be divided into microfibrils (<100 nm in diameter) and nanofibrils (1.5-3.5 nm in diameter). At a finer scale, these elementary fibrils are comprised of linear and stiff cellulose molecular chains, which are assembled from repeated units of D-glucose through covalent bonding and intra/interchain hydrogen bonding[15, 16]. Through the esterification reaction, CA can be obtained by replacing some of the hydroxyl groups on the cellulose chain with acetyl groups[17]. This derivative of cellulose, CA, possesses an enriched storage capacity and is inherently biodegradable. Consequently, CA offers a sustainable and eco-friendly alternative.

Supplementary Fig. 7. IR photograph of the CA and MXene films on a simulated skin heater.

To visually demonstrate the emissivity disparities between the CA and MXene, the CA and MXene films are stuck on a simulated skin heater with a constant temperature of 35 °C and characterized with an IR imager camera. Despite the identical surface temperature of around 35 °C, the MXene film appears much cooler than the CA film in the IR image. This divergence can be attributed to the marked contrast in emissivity between CA, which displays high emissivity, and MXene, which conversely possesses low emissivity.

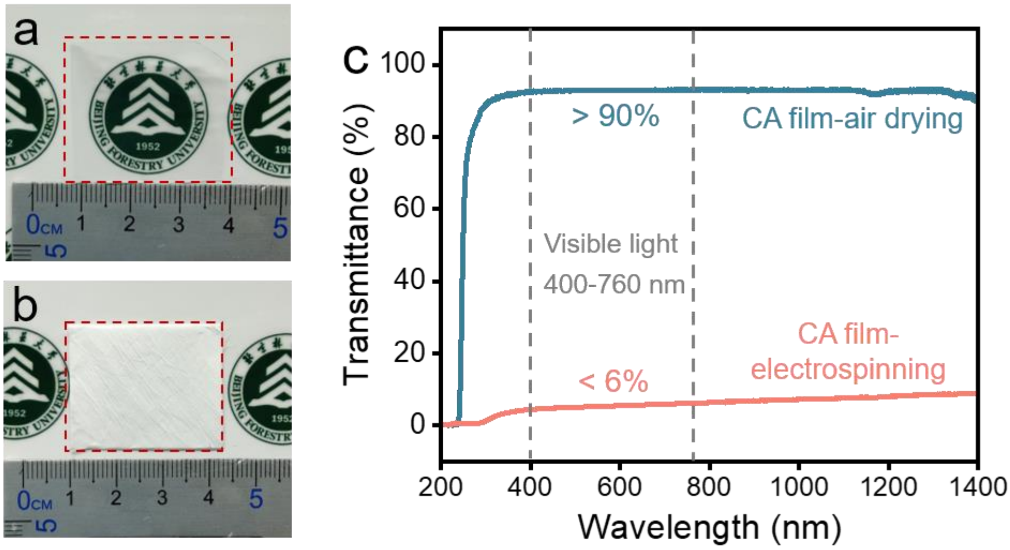

Supplementary Fig. 8. **Transmittance changes of CA films with different preparation methods. a** Photo of CA film prepared by natural air drying. **b** Photo of CA film prepared by electrospinning. **c** Spectral transmittance of the corresponding films in the range of solar spectrum from 200 to 1400 nm.

CA powder is dissolved in acetone/DMAC [2:1 (w/w)] to form a clear solution, followed by natural air-drying and electrospinning to yield two distinct CA films. In contrast to the transparent nature of the air-dried CA film, the electro spun CA film has negligible transmittance (<6%) within the visible light band because its many pores can efficiently scatter visible light, which benefits privacy protection[5].

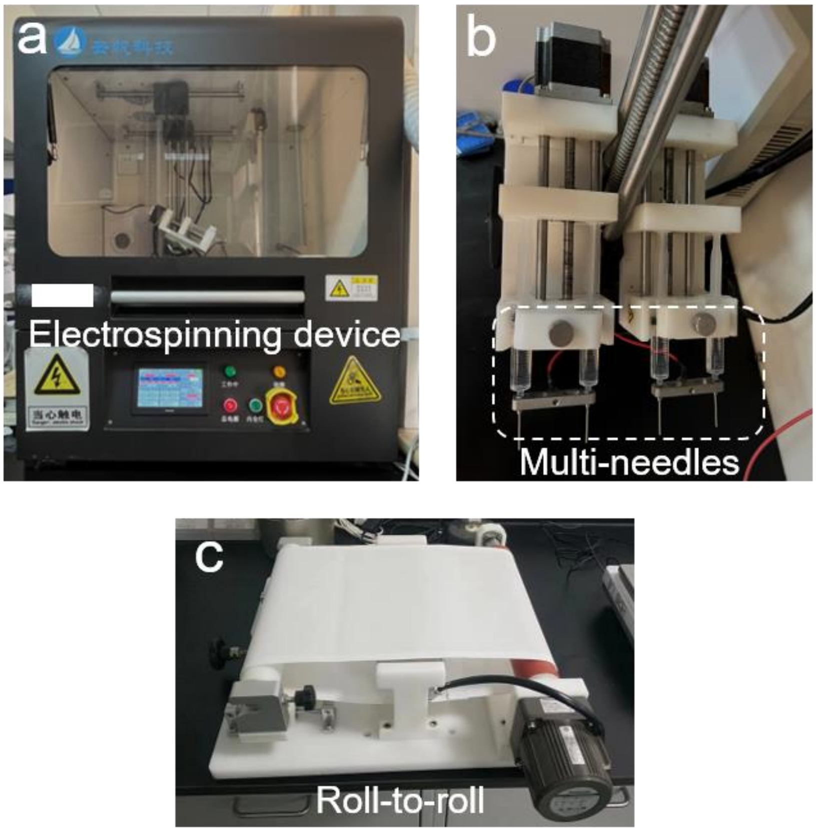

Supplementary Fig. 9. The image of **a** electrospinning device, **b** multi-needles, and **c** roll-to-roll equipment.

A photograph of the electrospinning device employed in the creation of the i-textile is provided (Supplementary Fig. 9a). Multi-needles increase the output of the CA fibers while accelerating the overall production of the i-textile (Supplementary Fig. 9b). Furthermore, the custom-made roll-to-roll equipment enhances the size of i-textile up to 0.3 × 1.2 m (Supplementary Fig. 9c).

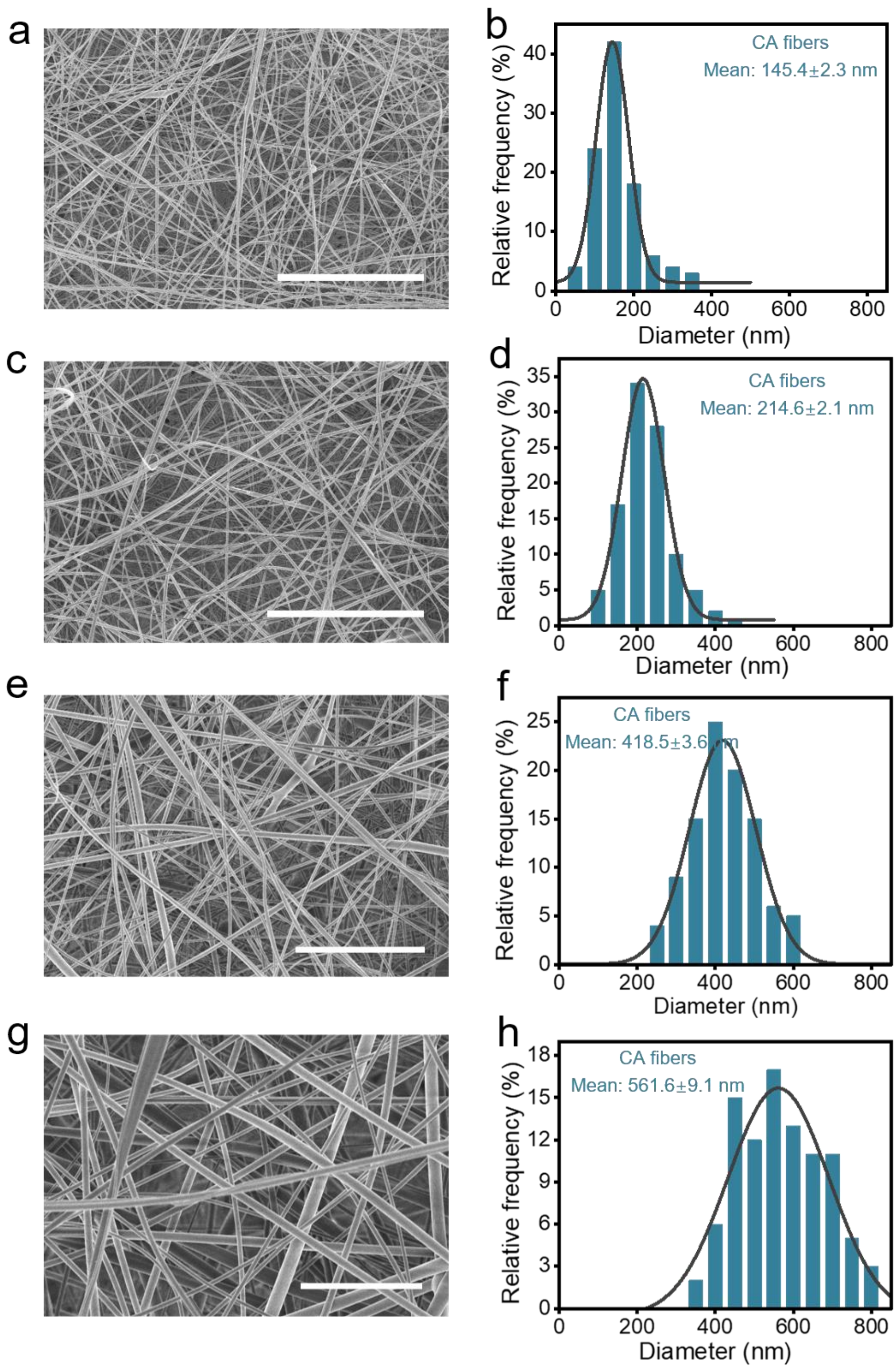

Supplementary Fig. 10. SEM images and fiber diameter distribution for **a-b** CA fiber-10.0, **c-d** CA fiber-12.5, **e-f** CA fiber-17.5, and **g-h** CA fiber-20.0. CA fiber-x, where x represents the mass fraction of CA powder in the acetone/DMAC solution. The scales are 15 μm.

The micrographs in Supplementary Fig. 10 depict the nanofiber morphology under various concentrations of CA at an applied voltage of 18 kV. Notably, at this voltage setting, the nanofibers display commendable morphology, exhibiting an absence of conspicuous beading or inter-fiber bonding. Upon incrementing the mass fraction of CA powder from 10.0 to 12.5, 17.5, and 20.0 wt%, a corresponding increase in the average nanofiber diameter is observed, measuring 145.4 nm, 214.6 nm, 418.5 nm, and 561.6 nm, respectively. This trend can be attributed to the escalating polymer concentration, which imparts heightened viscous resistance to the polymer solution. Consequently, the ability of the jet against the elongating force of the electric field intensifies, rendering the process of thinning the fibers more challenging. As a result, the fiber diameter undergoes a gradual augmentation.

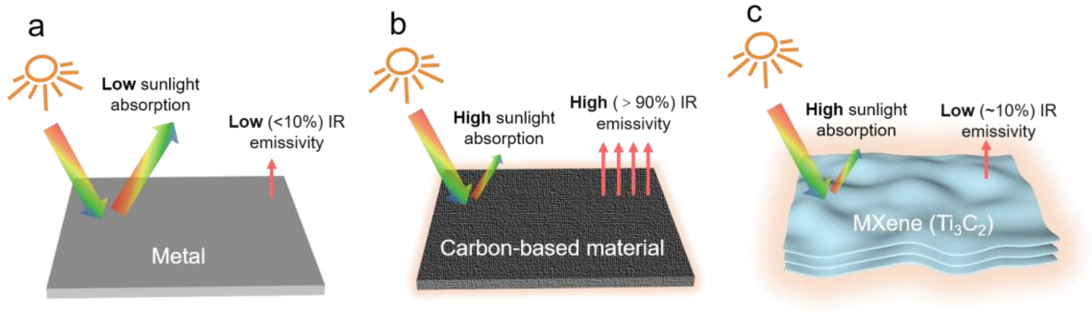

Supplementary Fig. 11. Light-matter interaction of metals, carbon-based blackbodies, and MXenes. a The low sunlight absorptance and low IR emissivity of metals. **b** The high sunlight absorptance and high IR emissivity of carbon-based blackbodies. **c** The high sunlight absorptance and low IR emissivity of MXene.

As widely acknowledged, metals generally possess high sunlight reflection over an ultra-broad band due to their high damping constant and low refractive index (Supplementary Fig. 11a). In contrast, most of the black materials such as carbon-based absorbers have strong sunlight absorption (Supplementary Fig. 11b). However, the blackbody-like absorber is not an ideal solar absorber, since most of the harvested solar energy dissipates via high thermal radiation emissivity. Unlike metals and blackbodies, MXene not only exhibits high sunlight absorption comparable to that of the carbon-based absorber, but their low IR emissivity allows for better storage of the harvested solar energy (Supplementary Fig. 11c)[18].

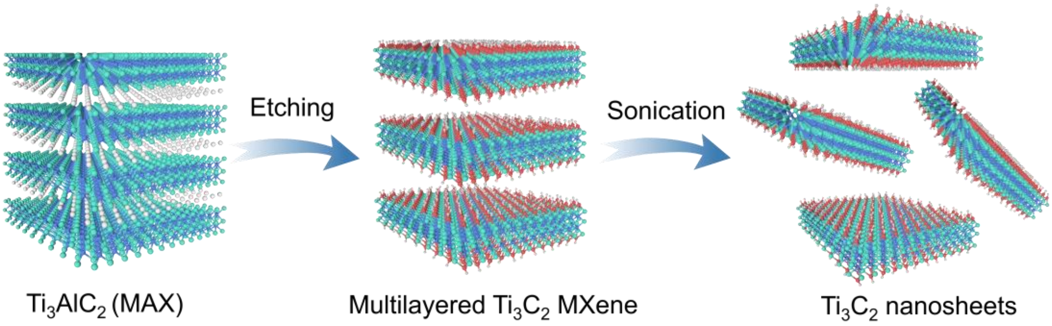

Supplementary Fig. 12. Schematic illustration of the fabrication of Ti_3C_2 nanosheets.

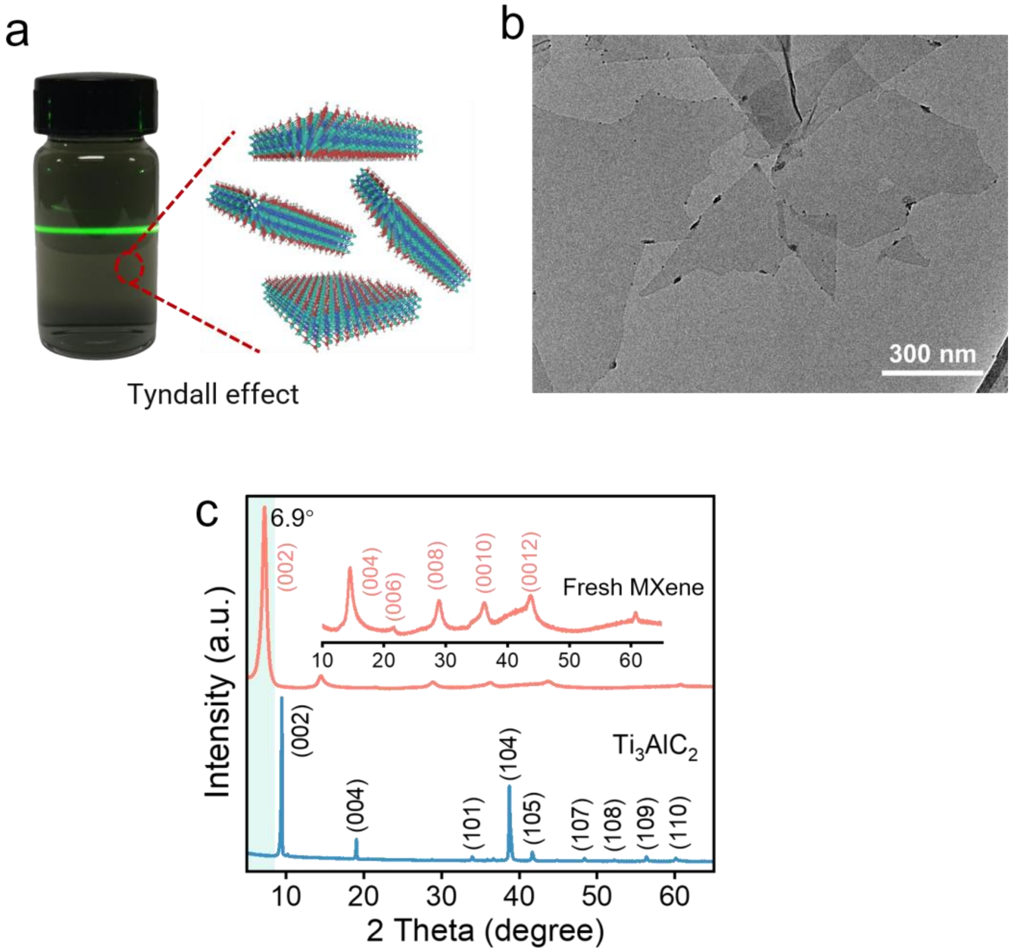

Supplementary Fig. 13. **a** Photograph of the Ti_3C_2 nanosheets aqueous dispersion and its typical Tyndall effect. **b** TEM image of the Ti_3C_2 nanosheets. **c** XRD patterns of Ti_3AlC_2 MAX powders and MXene.

Supplementary Fig. 13a presents the superior dispersity and hydrophilicity of the Ti_3C_2 nanosheets in deionized water by the typical Tyndall scattering effect. Fresh Ti_3C_2 MXene has a typical nanosheet morphology with a flat surface (Supplementary Fig. 13b)[19]. After chemical etching and delamination, the characteristic peak (002) is shifted from 9.5° of Ti_3AlC_2 powder to 6.9° of Ti_3C_2 nanosheets[20], indicating the successful conversion from Ti_3AlC_2 MAX phase to Ti_3C_2 nanosheets in XRD patterns (Supplementary Fig. 13c).

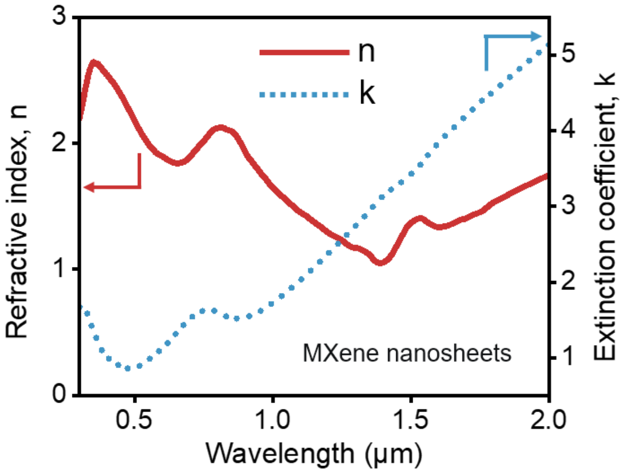

Supplementary Fig. 14. The complex spectral refractive index (n+ ik) of Ti_3C_2 nanosheets film in the solar wavelength range.

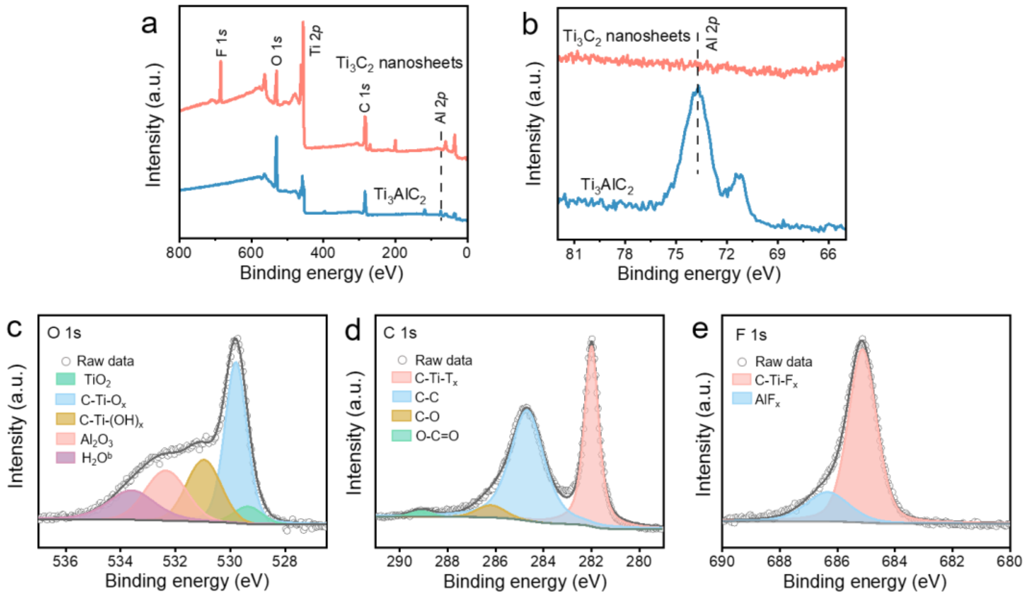

Supplementary Fig. 15. **XPS spectrum of Ti_3C_2 nanosheets. a-b** XPS spectrum of the Ti_3AlC_2 MAX powders and MXene nanosheets. **c-e** High resolution XPS spectra of O 1s, C 1s, and F 1s of the MXene nanosheets.

The XPS results verify the presence of Ti, C, O, and F in Ti_3C_2 nanosheets (Supplementary Fig. 15a). The disappearance of the typical Al 2p peak at 73.8 eV in Ti_3C_2 nanosheets illustrates that the Al layer in Ti_3AlC_2 MAX powders is successfully removed (Supplementary Fig. 15b). The deconvoluted C 1s spectrum of Ti_3C_2 nanosheets shows four major characteristic peaks at 282.0, 284.7, 286.2, and 289.1 eV, which are assigned to C−Ti, C−C, C−O, and O−C=O, respectively (Supplementary Fig. 15d). From their high-resolution XPS spectra, three typical types of terminal groups are identified in the Ti_3C_2 nanosheets including oxide (−O−), hydroxyl (−OH), and fluoride (−F, Supplementary Fig. 15c-e)[18].

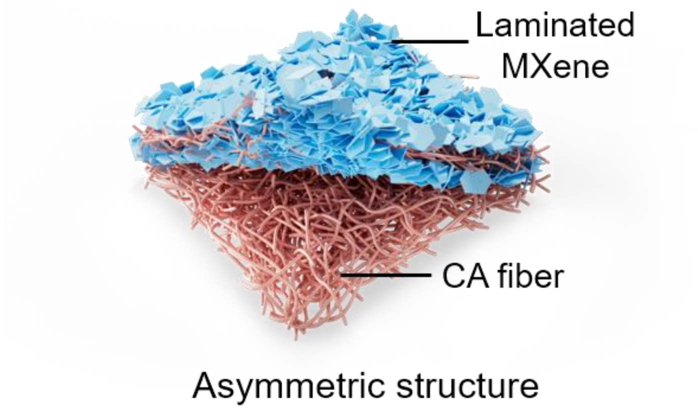

Supplementary Fig. 16. Schematic diagram of the i-textile.

Utilizing a roll-to-roll electrospinning technique, an innovative approach is employed to create i-textile featuring an asymmetric structure, combining CA and MXene components. In this design, CA nanofibers serve as a substrate covered with MXene nanosheets, forming a heating layer with remarkable sunlight absorption capabilities and low thermal radiation emission properties. Meanwhile, the cooling layer comprises pure CA nanofibers, efficiently reflecting sunlight and emitting human body thermal radiation.

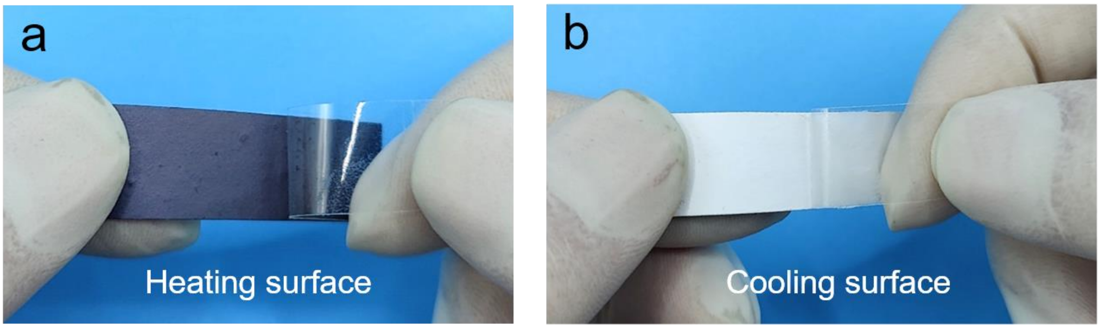

Supplementary Fig. 17. Adhesion test of **a** heating and **b** cooling surfaces of i-textile by adhesive tape.

Our study reveals that even after undergoing peeling by adhesive tape, MXene nanosheets on the heating surface remain structurally intact, underscoring their robust adhesion to CA nanofibers (Supplementary Fig. 17a). The adhesion test also shows that the heating surface is strongly bonded with the cooling surface and cannot be removed by adhesive tape (Supplementary Fig. 17b).

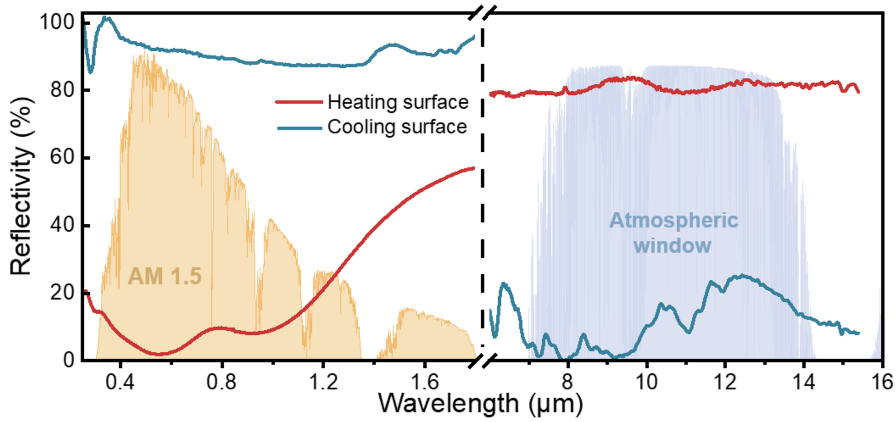

Supplementary Fig. 18. Sunlight and thermal radiation reflectivity of the i-textile. The yellow area denotes the spectra of solar irradiance and the purple area denotes the atmospheric window.

The optical properties of the i-textile are measured using Fourier transform infrared (FTIR) and ultraviolet-visible-near-infrared spectroscopy with an integrating sphere. The recorded spectra demonstrate that the heating surface exhibits low reflectivity across the solar spectrum, accompanied by high reflectivity within the atmospheric window range. When flipped, the cooling surface showcases high solar reflectivity and low reflectivity within the atmospheric window.

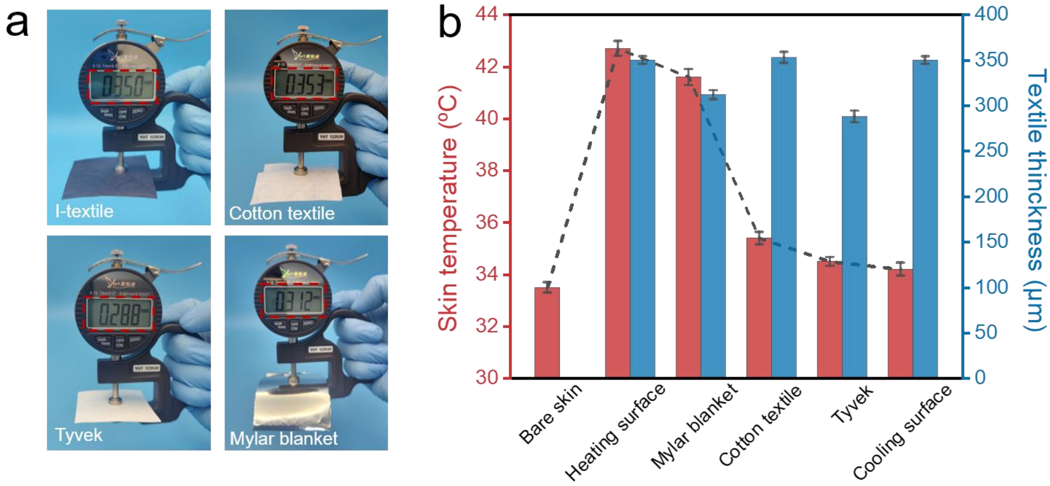

Supplementary Fig. 19. a Measured thickness of i-textile, cotton textile, Tyvek, and Mylar blanket. **b** Final temperature of the simulated skin covered with different textiles after 30 min of an indoor experiment.

The temperature of the simulated skin is regulated through the precise adjustment of direct current voltage, while concurrently monitoring the real-time temperature of the simulated skin covered with various textiles. When the i-textile's heating surface faces outward, the temperature of the simulated skin covered with i-textile reaches 42.7 °C, surpassing that of cotton textile and commercial heated material (Mylar blanket) by 7.3 and 1.1 °C, respectively. Conversely, when the i-textile's cooling surface is positioned outward, the temperature of the simulated skin registers at 34.2 °C, representing a 1.2 and 0.3 °C reduction compared to that of cotton textile and commercially cooling material (Tyvek), respectively.

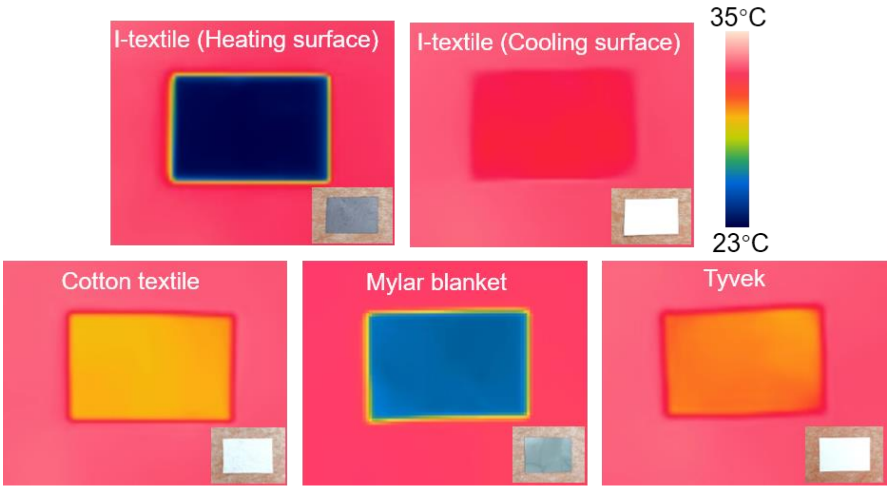

Supplementary Fig. 20. Infrared images of the heating and cooling surfaces of i-textile, cotton textile, Mylar blanket, and Tyvek covering the simulated skin.

To visualize the infrared emissivity of various textiles, a thermal camera is employed to detect the infrared radiation from a simulated skin covering with different textiles. In thermal imaging, colder colors indicate less emission of radiative heat. The color comparison here reveals that the simulated skin emits minimal infrared heat when the i-textile heating surface faces outward (colder color), while the cooling surface emits infrared heat to the environment substantially (warmer color). Comparatively, when juxtaposed with other materials, the heating surface of the i-textile exhibits the lowest emissivity, while the cooling surface displays the highest emissivity. This unique property equips the i-textile to effectively fulfill indoor personal heating and cooling requirements.

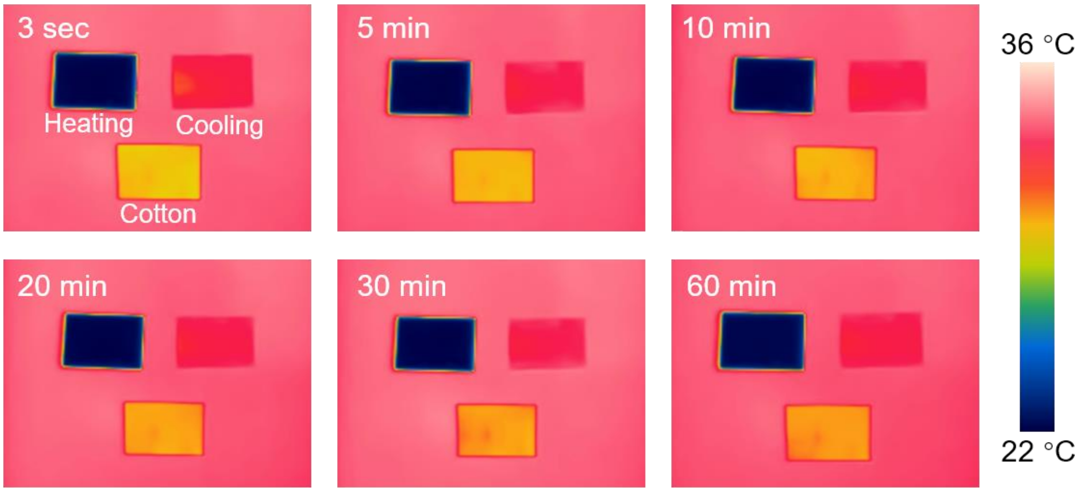

Supplementary Fig. 21. Infrared images of the heating and cooling surface of i-textile and cotton textile at 3 seconds, 5 minutes, 10 minutes, 20 minutes, 30 minutes, and 60 minutes on a simulated skin.

As illustrated in Supplementary Fig. 21, our i-textile, which is covered on a simulated skin for 60 minutes, consistently retains its distinct high (cooling surface) and low (heating surface) emissivity characteristics.

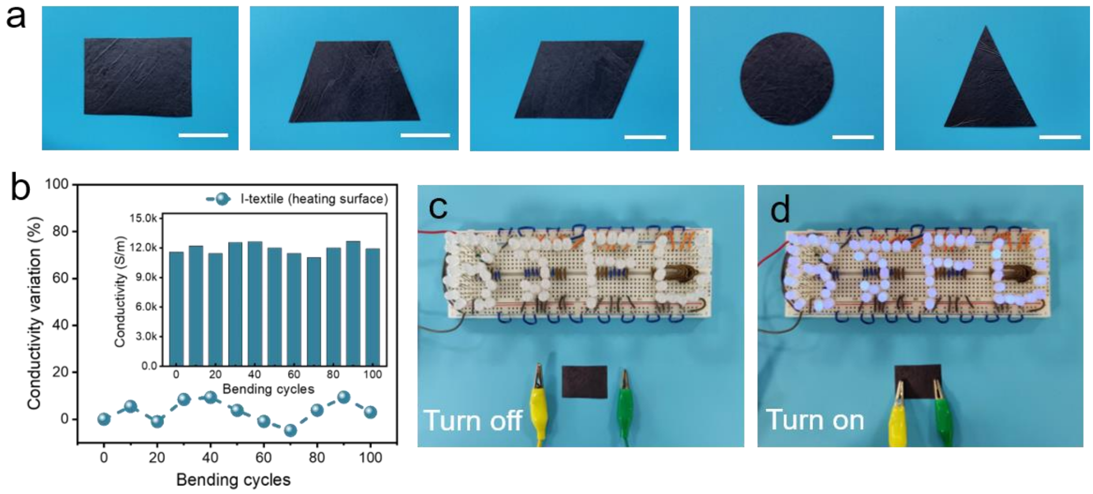

Supplementary Fig. 22. a The i-textile can be cut into different shapes. The scales are 1 cm. **b** The conductivity variation of i-textile after 100 times of bending. Inset: the conductivity value of i-textile after 100 times of bending. **c-d** Photograph of i-textile as a flexible conductor for lighting a blue LED lamp pattern.

The i-textile can be cut into different shapes to cater to diverse scenarios (Supplementary Fig. 22a). Its exceptional conductivity, exceeding 10,000 S/m, coupled with its inherent flexibility, positions it as a promising candidate for applications in conductive textiles. We rigorously investigate its conductive stability following 100 bending deformations (Supplementary Fig. 22b). Notably, the conductivity of the i-textile exhibits only negligible changes. In practical applications within the realm of electrical textiles, the textile was seamlessly connected to an ensemble of LED beads pattern group using copper wire. After the power is switched on, the LED beads patterns of "BJFU" are lighted (Supplementary Fig. 22c-d).

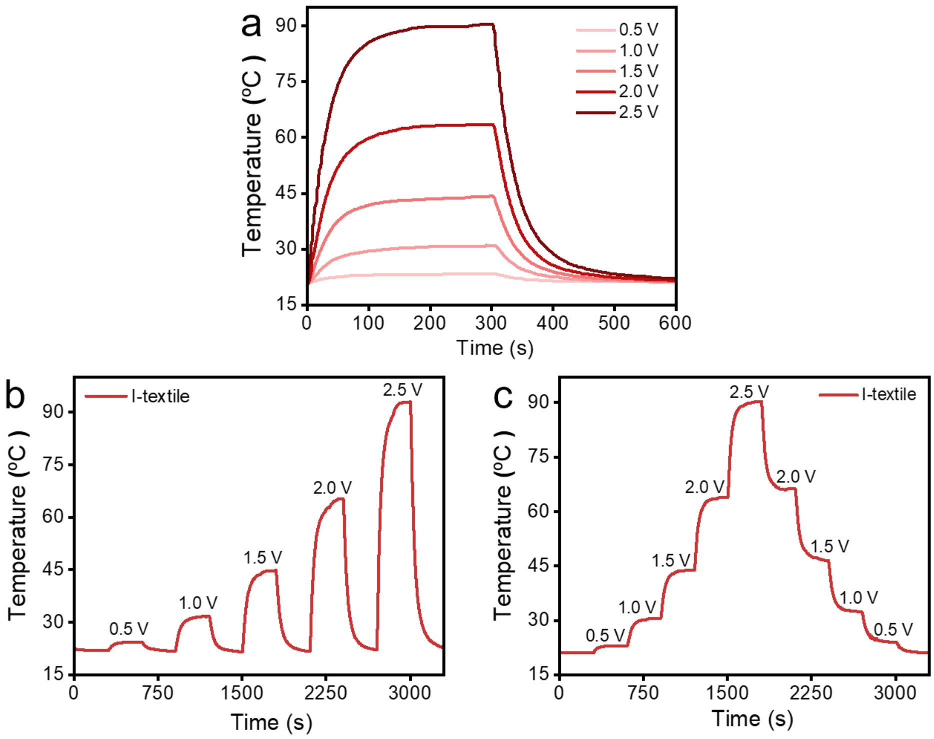

Supplementary Fig. 23. **Electrothermal performance of i-textile.** Temperature profiles of i-textile **a** as a function of time at different voltages **b** under a stepwise voltage from 0 to 2.5 V **c** from 0 to 2.5 V and from 2.5 to 0 V by adjusting the applied voltage.

The i-textile demonstrates outstanding Joule heating capabilities, which can be used as a supplement to cope with a complicated heating environment[21], such as a cold winter or a rainy day in an indoor environment. After a safe voltage of 0.5, 1.0, 1.5, 2.0, and 2.5 V is applied, the temperature of the i-textile reaches 23.4, 31.0, 44.3, 63.5, and 90.6 °C, respectively (Supplementary Fig. 23a). Supplementary Fig. 23b shows the temperature profiles of the i-textile under stepwise voltage from 0 to 2.5 V. It is evident that the textile's temperature increases with increasing input voltage. Notably, when a continuous input voltage of 2.5 V is maintained, the i-textile rapidly attains a peak temperature of 92.6 °C within a mere 300 s, underscoring its exceptional thermal responsiveness and efficient electric-to-heat conversion. Furthermore, the Joule heating performance of i-textile is sensitive and adjustable, which can be switched from 0 to 2.5 V or from 2.5 to 0 V easily to obtain a desired heating temperature (Supplementary Fig. 23c).

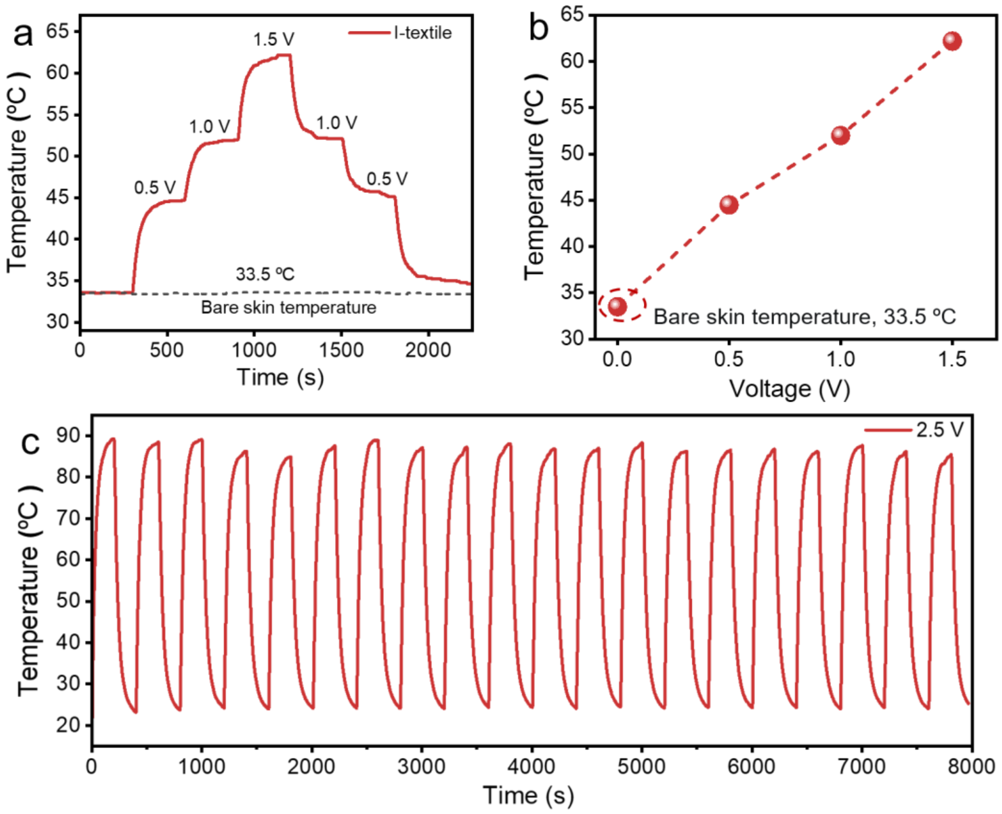

Supplementary Fig. 24. a Temperature profiles and **b** temperature points of simulated skin covered with i-textile under a voltage ranging from 0 to 1.5 V. **c** Temperature-time curve of i-textile under a 2.5 V input voltage for 20 cycles.

By adjusting the voltage within the range of 0 to 1.5 V, the temperature of the simulated skin covering the i-textile will increase or decrease (Supplementary Fig. 24a). Notably, under a 1.5 V voltage input, the skin temperature achieves a significant peak of 62.2 °C, surpassing the temperature observed in the non-heating mode (Supplementary Fig. 24b). To further evaluate the electrothermal stability, the recycling temperature variations of the i-textile are recorded under a 2.5 V input voltage for 20 on/off cycles (Supplementary Fig. 24c). The Joule heating performance of the i-textile does not show any significant deterioration during the cycling process, demonstrating superior electrothermal stability. The highest input voltage (2.5 V) used in this work is also much lower than the standard safe voltage (36 V) of the human body, indicating the safety and reliability of the electrical heaters[22]. Taken together, these findings unequivocally demonstrate that the i-textile exhibits outstanding Joule heating performance.

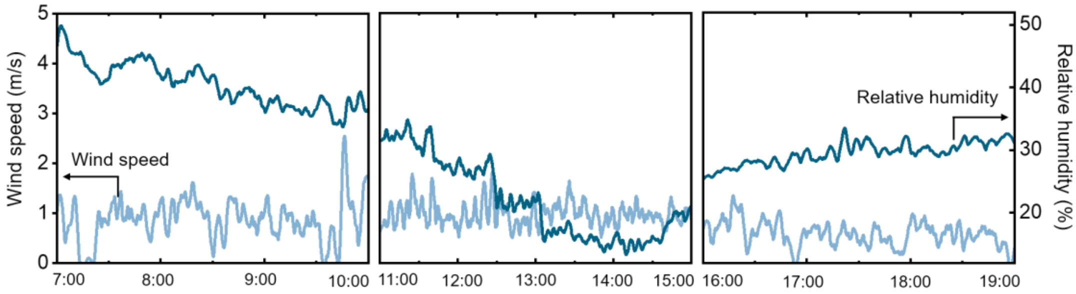

Supplementary Fig. 25. The real-time wind speed and relative humidity on a sunny day (22 May 2023).

In the test process, the wind speed consistently maintains a low and stable level, rarely exceeding 2 m/s. Relative humidity initially registers at high levels, gradually declines to a minimum before gradually rebounding.

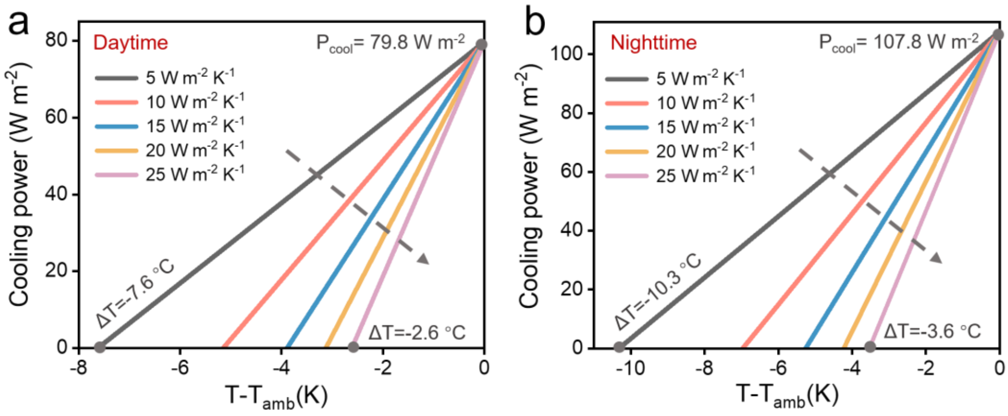

Supplementary Fig. 26. Curve of theoretical radiative cooling power and temperature for i-textile during **a** daytime and **b** nighttime.

To better understand the cooling performance of the i-textile, we systematically study its cooling power during the daytime and nighttime based on the calculated emissivity. The i-textile is affected by solar irradiance and atmospheric thermal radiation when exposed to an outdoor environment during the daytime, while solar irradiation can be ignored at nighttime. In addition, heat can be transferred from the surrounding environment to the textile utilizing heat conduction and convection due to the temperature difference between the textile and the surrounding environment. Considering the above factors, we calculate the radiative cooling power of the i-textile through thermal relation as described in Supplementary Note 1, assuming that the ambient temperature T_{amb} is 25 °C and the nonradiative thermal transfer coefficient (h_c) is 5, 10, 15, 20, and 25 W m^{-2} K^{-1}. As shown in Supplementary Fig. 26 a and b, the theoretical cooling power of i-textile reaches 79.8 W m^{-2} and 107.8 W m^{-2} during the daytime and nighttime, respectively. Notably, P_{cool} is defined as the net cooling power when $T = T_{amb}$, which is not affected by nonradiative thermal transfer. When P_{cool}= 0, $(T - T_{amb})$ is the maximum achievable cooling temperature. As shown in Supplementary Fig. 26, the maximum cooling temperature decreases with the increase of the nonradiative thermal transfer coefficient.

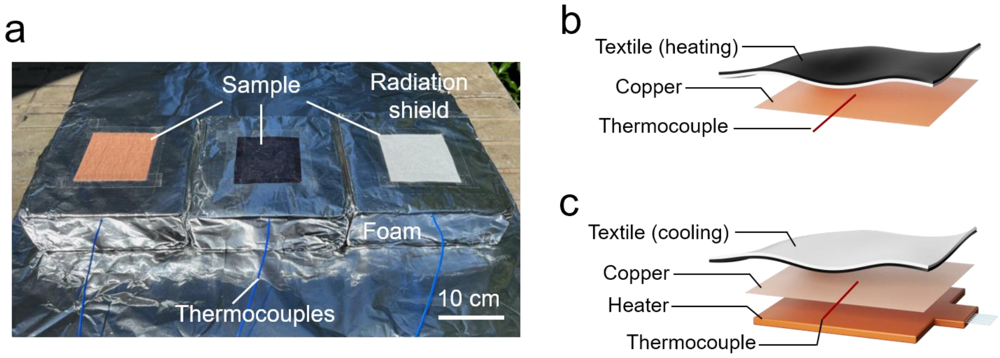

Supplementary Fig. 27. Direct thermal analysis to determine the thermoregulatory performance. a A photograph shows the setup used for monitoring the temperatures of samples under sunlight. Schematic of the setup used for the **b** ambient test and **c** skin simulator test.

Our measurement setup utilizes polystyrene foam to isolate ambient heat and an aluminum film to reflect sunlight (Supplementary Fig. 27a). Supplementary Fig. 27b-c illustrates the inner workings of the measurement setup. The temperature of each textile is monitored by thermocouples taped on the copper plate to ensure the accuracy and uniformity of thermal measurements (Supplementary Fig. 27b). We conduct tests to evaluate the thermoregulatory performance of our i-textile using a human skin simulator (Supplementary Fig. 27c).

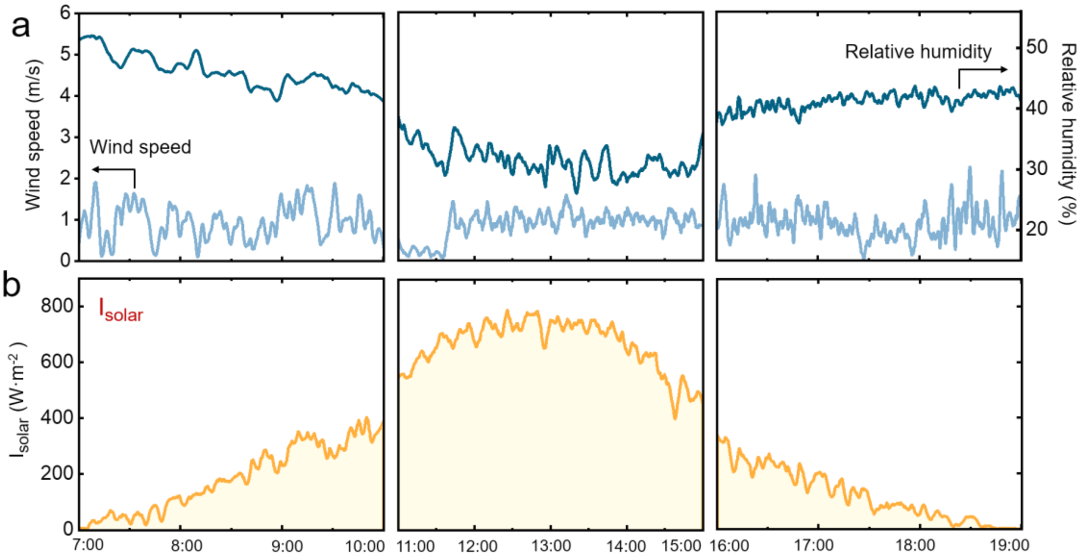

Supplementary Fig. 28. The real-time wind speed, relative humidity, and solar intensity on a sunny day (7 May 2023).

During the test process, the wind speed consistently maintains a low and stable level, seldom exceeding 2 m/s (Supplementary Fig. 28a). Solar radiation intensity initiates at a low level and progressively ascends to its peak before gradually diminishing. The peak solar radiation intensity reaches ~770 W m^{-2} (Supplementary Fig. 28b). In response to fluctuations in solar irradiation intensity, relative humidity exhibits a pattern of initially commencing at high levels, followed by a gradual decline to a minimum, and subsequently showing an incremental increase.

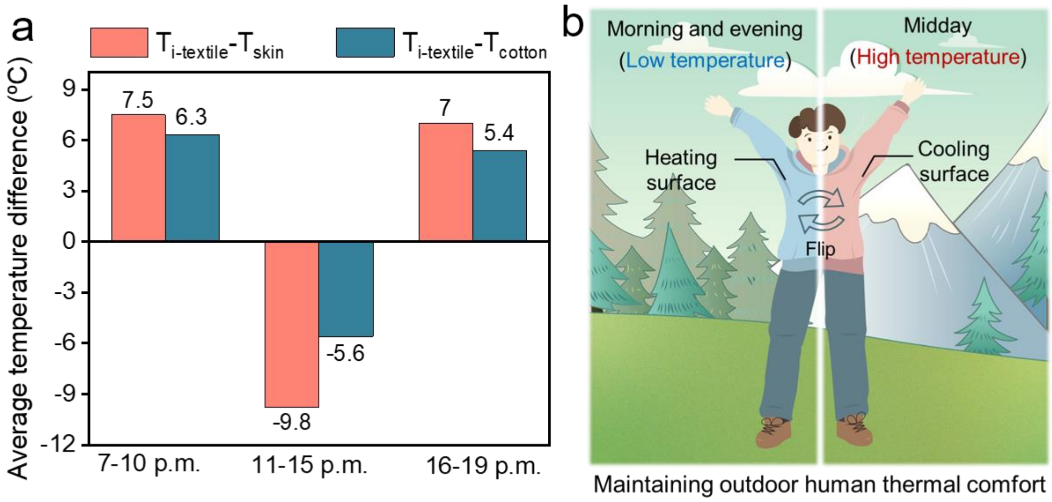

Supplementary Fig. 29. a The average temperature differences between simulated skin covered with i-textile and bare skin (orange column) and between simulated skin covered with i-textile and skin covered with cotton textile (blue column). **b** Schematic of a human wearing i-textile in an outdoor environment.

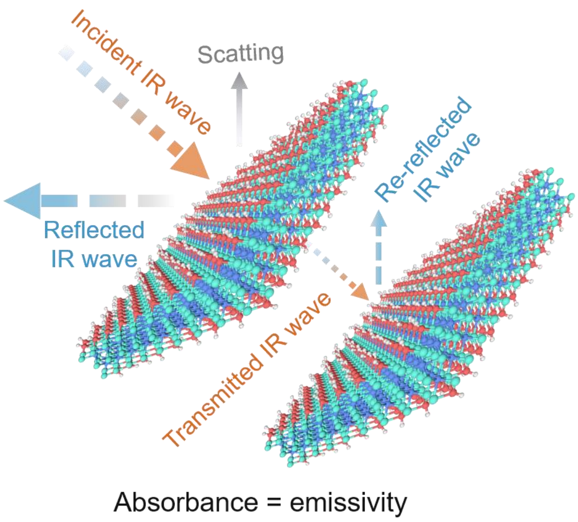

Supplementary Fig. 30. Schematic illustration of the proposed low IR emissivity of MXene.

As illustrated in Supplementary Fig. 30, the low infrared emissivity arises from its high reflectivity. According to the Hagen-Rubens theorem, the electrical conductivity of an object is essentially synonymous with the reflection coefficient in the infrared range. As the infrared waves hit the exposed surface of the MXene, the majority of energy is reflected directly and cannot reach the inside because MXene is extremely conductive. The survived infrared waves also suffer from re-reflection by the inner flakes[23].

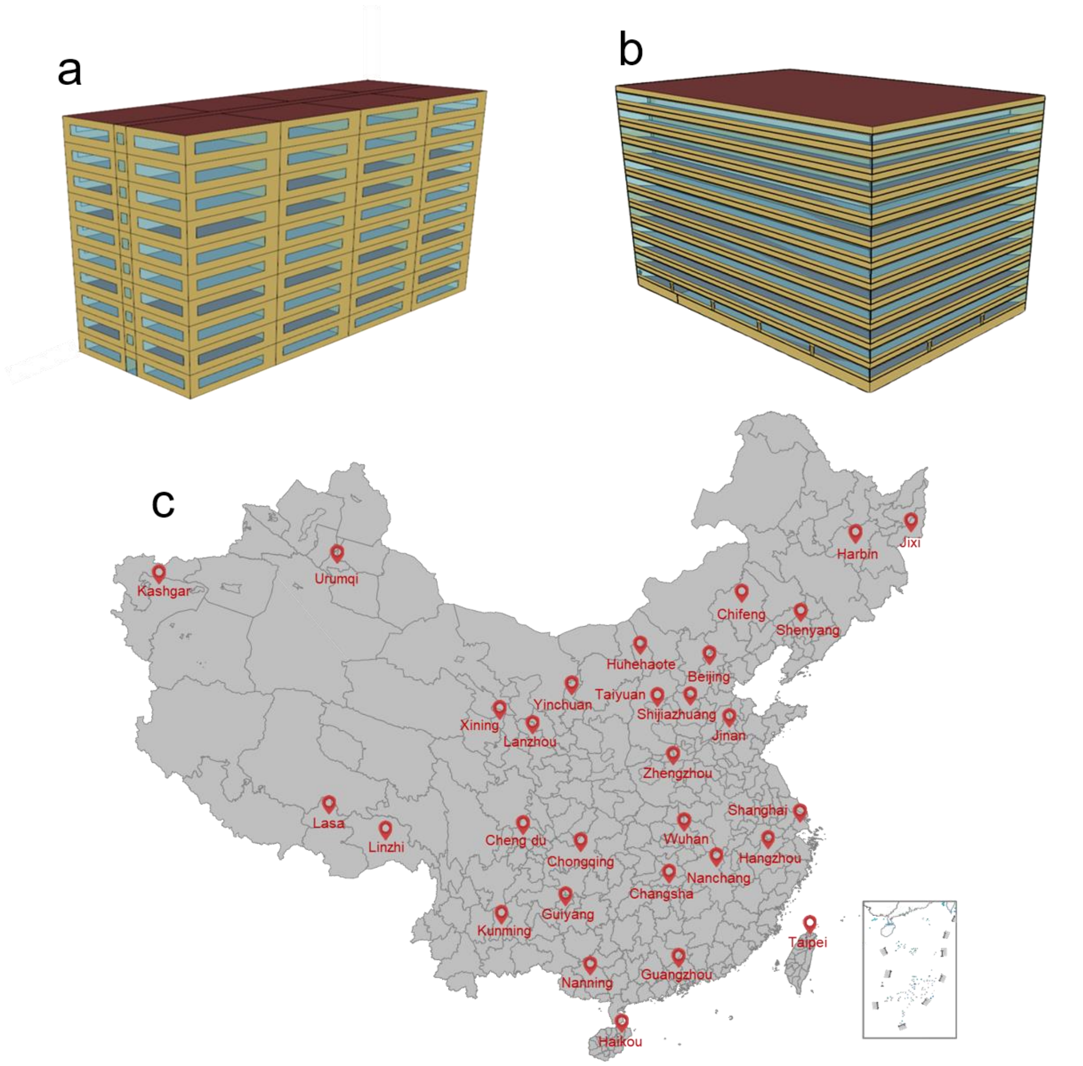

Supplementary Fig. 31. Building energy simulation. Schematic of **a** apartment and **b** office buildings. **c** The 30 cities in China assessed for energy savings for apartment and office buildings.

Among the various building types, apartment and office buildings stand out as the most prevalent choices for residents (Supplementary Fig. 31a and b). Consequently, our simulation focuses on these two predominant building types. In this simulation, we choose a set of 30 cities from across the nation, carefully selected to represent all 7 distinct building climate zones in China (Supplementary Fig. 31c).

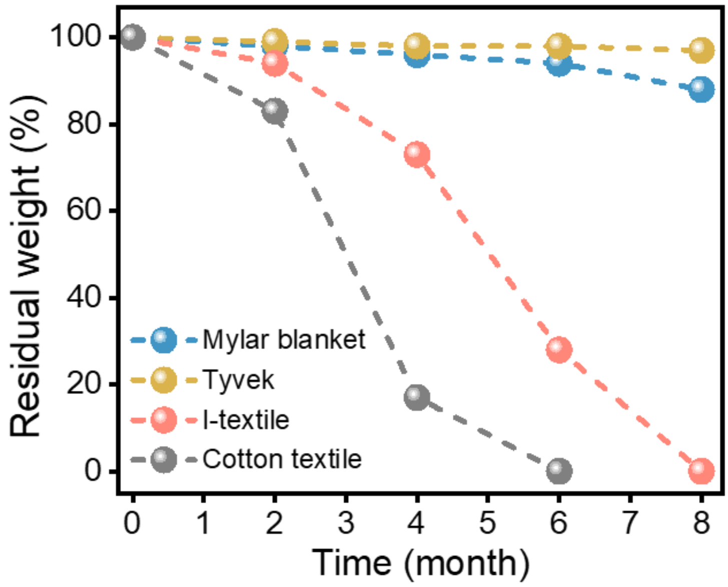

Supplementary Fig. 32. Residual weight of the Mylar blanket, Tyvek, i-textile, and cotton textile as a function of time in soil.

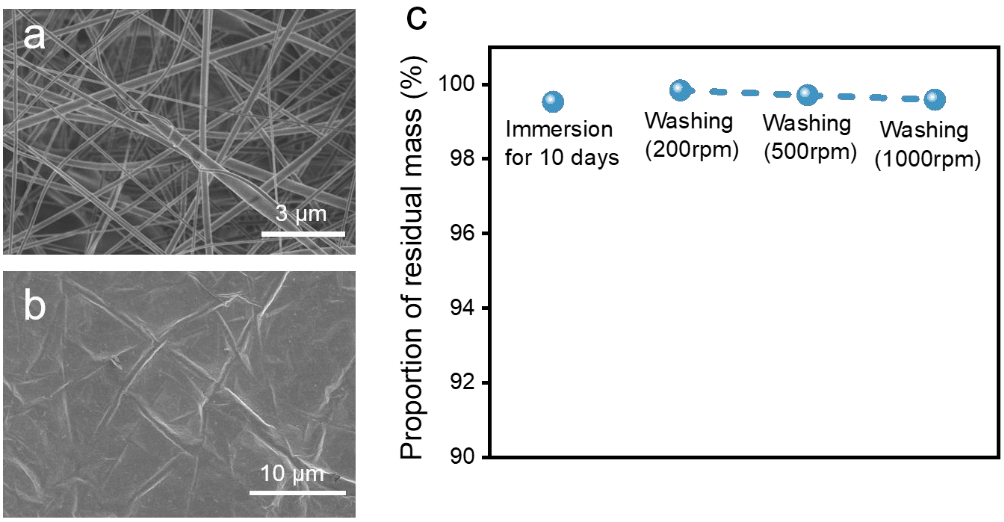

Supplementary Fig. 33. The SEM images of **a** cooling and **b** heating surfaces of i-textile after washing under ultrahigh speed (1000 rpm) stirring for 30 min. **c** The proportion of residual mass of i-textile after washing under medium speed (200 rpm), high speed (500 rpm), and ultrahigh speed (1000 rpm) stirring, respectively.

SEM images of the cooling and heating surfaces reveal that the morphology remains unchanged even after undergoing washing. After immersing and washing under various speeds in water, the i-textile exhibits a negligible mass loss, accounting for a mere 0.5% of its total mass.

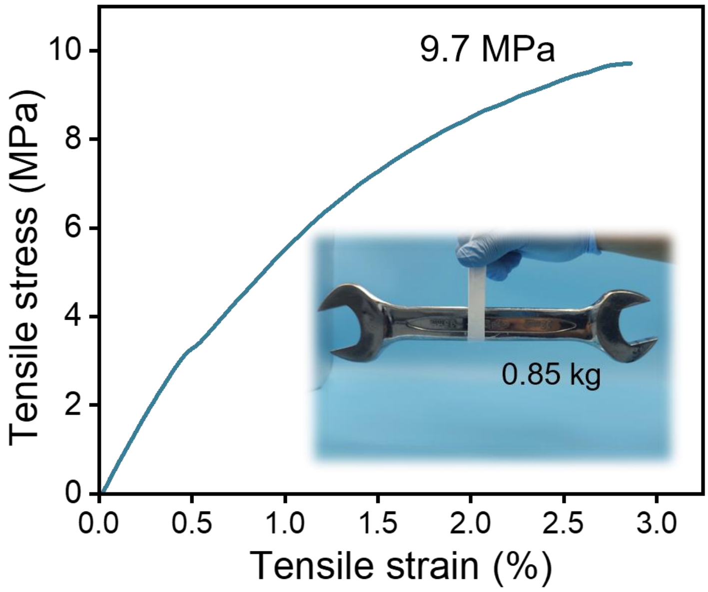

Supplementary Fig. 34. Tensile strength of i-textile. Inset: The i-textile has the capability to elevate a wrench with a mass of 0.85 kg.

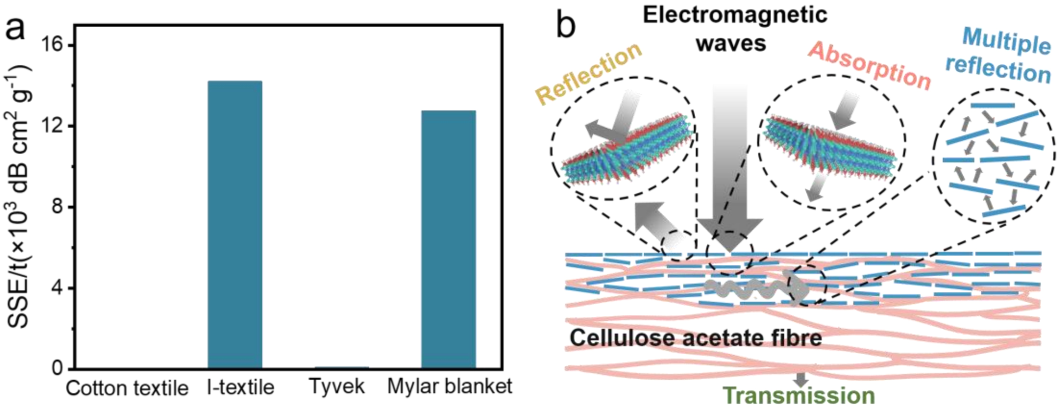

Supplementary Fig. 35. a Comparison of EMI SSEt of various textiles. **b** Schematic illustration of the EMI wave shielding mechanism of i-textile.

The potential EMI attenuation mechanisms of i-textile are presented in Supplementary Fig. 35b. As the incident electromagnetic wave strikes the i-textile, a part of the electromagnetic wave is reflected back owing to the abundant free electrons at the top surface layer of the conductive MXene (the first layer)[24]. The remaining waves pass through the d-$Ti_3C_2T_x$ lattice structure and interact with the high charge density d-$Ti_3C_2T_x$, resulting in a significant reduction of the wave energy. Then, the surviving waves strike the CA/MXene mutual mixed matrix (the middle layer). In this layer, MXene nanosheets with an irregular layered stacking structure can provide more interfaces for repeated reflection and adsorption. Under the synergistic effect of two conductive layers containing MXene nanosheets, the i-textile can achieve outstanding EMI shielding performance.

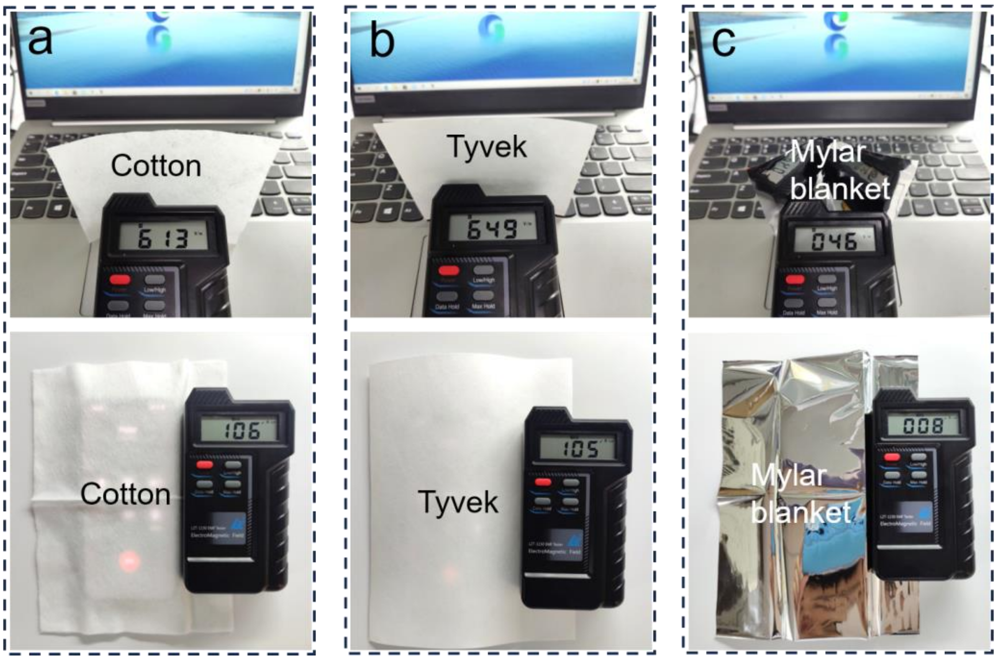

Supplementary Fig. 36. The practical application of the electromagnetic interference shielding performance of **a** cotton textile, **b** Tyvek, and **c** Mylar blanket in mobile phones and computers.

In our daily lives, humans are exposed to the potential risk of electromagnetic radiation emitted by electronic equipment. Fortunately, the i-textile exhibits exceptional EMI shielding performance due to its high electrical conductivity. Notably, the EMI efficiency of the i-textile within the entire X band surpasses 35 dB (Fig. 6j). This level of shielding exceeds the established civil standards for mitigating electromagnetic radiation. Both EMI SE and EMI shielding efficiency (SSE_t) values of the i-textile are comparable to that of Mylar blanket and significantly outperform those of cotton textile and Tyvek (Fig. 6j, Supplementary Fig. 35a). Furthermore, we conduct investigations into the practical application of these materials in electromagnetic shielding. The results indicate that when electronic devices such as computers and mobile phones are shielded with the i-textile, the recorded electromagnetic radiation values are notably lower than those of cotton textile and Tyvek, and slightly lower than that of Mylar blanket (Fig. 6j, Supplementary Fig. 36). This suggests that the i-textile exhibits outstanding electromagnetic shielding properties.

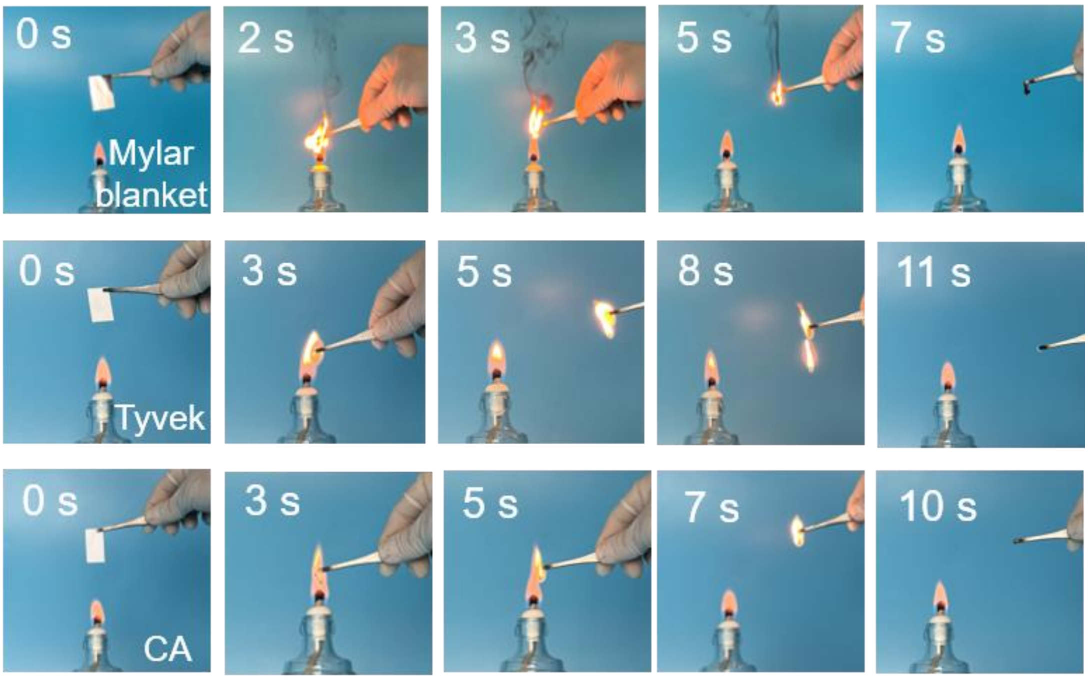

Supplementary Fig. 37. Combustion experiment of Mylar blanket, Tyvek, and CA in a hot flame.

The application of MXene coating of the i-textile yields a pronounced enhancement in the flame retardancy of this textile. This enhancement proves to be of paramount importance in facilitating the practical utilization of polymeric textiles. The samples of cotton textile, Mylar blanket, Tyvek and CA burn vigorously after being ignited and burn into melt dripping after ~ 10 s (Supplementary Fig. 37). In contrast, the i-textile displays exceptional fire resistance throughout the entire combustion process, remains virtually unburnt and devoid of any molten droplets (Figure 6l). This remarkable behavior can be attributed to the partial oxidation of MXene nanosheets to form TiO_2 following combustion[6]. Consequently, a continuous and dense TiO_2 layer is formed on the surface of the i-textile, effectively serving as a physical barrier that inhibits flame propagation and the formation of molten droplets, thus indicating the flame retardancy of the i-textile.

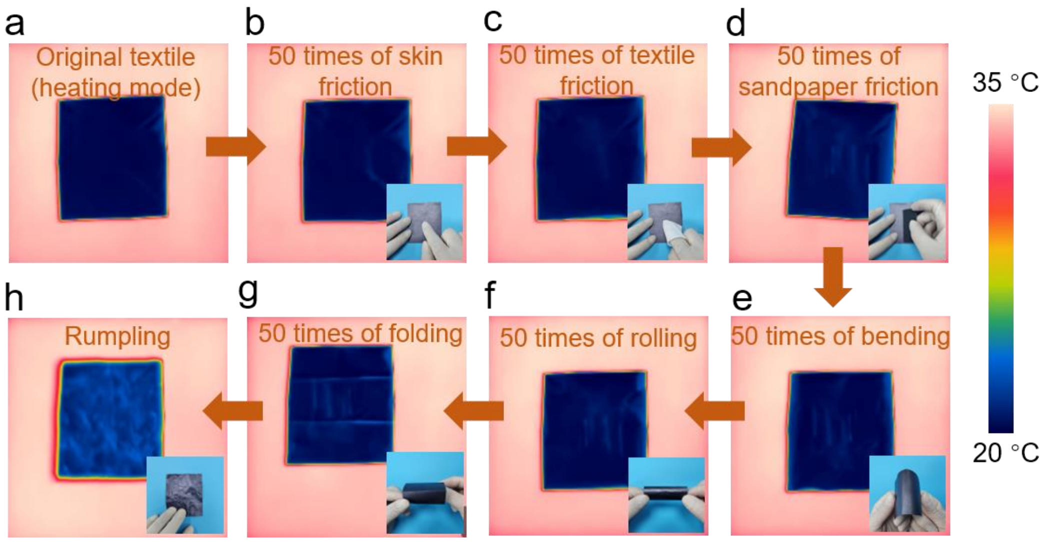

Supplementary Fig. 38. Thermal infrared images of **a** original heating surface of the i-textile in a hot state after **b** friction by skin, **c** friction by textile, **d** friction by sandpaper, **e** bending, **f** rolling, **g** folding, and **h** rumpling.

The heating surface of the i-textile undergoes successive frictional interactions with skin, textile, and sandpaper, followed by deformation through bending, rolling, folding, and rumpling, all while consistently retaining a low emissivity (Supplementary Fig. 38). This observation underscores the remarkable mechanical abrasion resistance of the i-textile.

Supplementary Fig. 39. Photographs of *E. coli* and *S. aureus* cultured on cotton textile and i-textile at 37 °C for 24 h after elution.

The antibacterial performance is important for wearable textiles and devices. MXene nanosheets have been confirmed to be able to penetrate bacteria to damage cell walls and plasma membranes, resulting in the death of bacteria due to a large amount of cytoplasmic components leaking from the bacteria[25]. Compared with cotton textile, the petri dishes impregnated with i-textile exhibit notably reduced growth of *E. coli* and *S. aureus*, underscoring its better antibacterial activity (Supplementary Fig. 39).

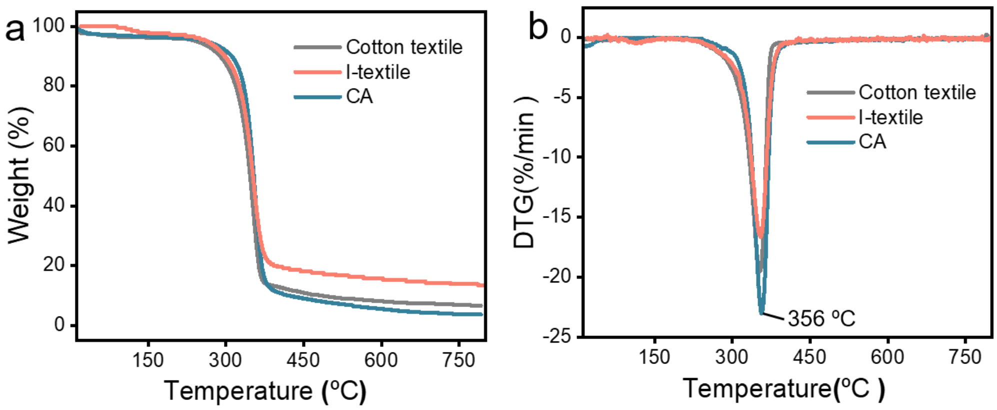

Supplementary Fig. 40. a TG and **b** DTG curves of cotton textile, i-textile, and CA.

The main thermal degradation of the i-textile is observed to transpire within the temperature range spanning from 280 to 380 °C (Supplementary Fig. 40a). Notably, the maximum weight loss rate is discerned precisely at 356 °C, as depicted in Supplementary Fig. 40b. Consequently, it can be deduced that the i-textile demonstrates remarkable thermal stability, effectively withstanding temperatures of up to 280 °C, thereby rendering it suitable for a wide array of wearable applications.

Table S1. Input parameters for the heat transfer model analysis.

Symbol	Definition	Value	Unit
q_{gen}	Metabolic heat generation flux	75	W m^{-2}
k	Thermal conductivity	Textile, k_t = 0.3 Air gap, k_a = 0.03	W m^{-1} K^{-1}
t	Thickness	Textile, t_t = 350 Air gap, t_a = 1200	μm
h	Natural convective heat transfer coefficient	4.1	W m^{-2} K^{-1}
σ	Stefan-Boltzmann constant	5.67×10^{-8}	W m^{-2} K^{-4}
ε	IR emittance	Skin, ε_s = 0.98 Environment, ε_e = 1 Cotton, ε_c = 0.77 Textile inner surface, ε_i Textile outer surface, ε_o	unitless
α	IR absorbance	Cotton, α_c = 0.77 Textile inner surface, $\alpha_i = \varepsilon_i$ Textile outer surface, $\alpha_o = \varepsilon_o$	unitless
τ	IR transmittance	Cotton, τ_c = 0.02 Opaque textile, τ_t = 0	unitless
ρ	IR reflectance	Cotton, ρ_c = 0.09 Textile inner surface, $\rho_i = 1 - \tau_t - \varepsilon_i$ Textile outer surface, $\rho_o = 1 - \tau_t - \varepsilon_o$	unitless
T	Temperature	Skin, T_s = 306.65 Environment temperature, T_e Textile inner surface, T_i Textile outer surface, T_o	K

Table S2. The collective metrics assessment among i-textiles and currently reported state-of-the-art PTM textiles.

Ref. (Published on)	Materials	Biodegradability	Solar absorption	Solar reflection	IR reflection	IR emissivity/ transparently	Joule heating	Washability	Electromagnetic shielding	Antibacterial	Flame retardant
Nat. Commun. 2017,8,496	PE/Ag/Cotton	✗	✗	✓	✓	✗	N/A	✓	N/A	N/A	N/A
Sci. Adv. 2017, 3, e1700895	PE/C/Cu	✗	✓	✗	✓	✓	N/A	✓	N/A	✗	N/A
Angew. Chem. Int. Edit, 2022, e202208592	PVDF-HFP/Ag/GO	✗	✓	✗	✓	✓	✓	✓	N/A	N/A	N/A
Nat. Nanotechnol. 2021, 16, 153–158	PEO	✗	✗	✓	✗	✓	✗	N/A	✗	✗	✗
Nat Sustain. 2018, 1, 105-112	Nano PE	✗	✗	✓	✗	✓	✗	✓	✗	✗	✗
Adv. Mater. 2018, 30, 1802152	PE/ZnO	✗	✗	✓	✗	✓	✗	N/A	N/A	N/A	N/A
Acs. Nano.2021,15, 11396-11405	Nano PE/MXene	✗	✓	✗	✓	✗	✓	✓	✓	✓	✓
Adv. Sci. 2022, 9, 2104758	CA	✓	✗	✓	✗	✓	✗	N/A	✗	✗	N/A
Adv. Sci. 2023, 10, 2206176	PMMA/Cotton-PPy	✗	✓	✓	✗	✓	N/A	N/A	N/A	N/A	N/A
Adv. Funct. Mater. 2022, 32, 2108808	PI/TPU/AgNW	✗	✗	✗	✓	✓	✓	✗	N/A	N/A	N/A
J. Mater. Chem. A,2021,9,25178–25188	Hollow AlPO4/CA	✓	✗	✓	✗	✓	✗	N/A	✗	N/A	N/A
Nano. Energy. 2022, 95, 106996	TiN NPs/Cotton/PTFE	✗	✓	✗	✓	✗	✓	✓	N/A	N/A	N/A
Chem. Ene. J. 2023, 466, 143127	Silk fibroin	✓	✗	✓	✗	✓	✗	N/A	✗	N/A	N/A
This work	CA/MXene (i-textile)	✓	✓	✓	✓	✓	✓	✓	✓	✓	✓

Reference

1. Cai, L. et al. Spectrally selective nanocomposite textile for outdoor personal cooling. *Adv. Mater.* **30**, 1802152 (2018).

2. Luo H, et al. Outdoor personal thermal management with simultaneous electricity generation. *Nano Lett.* **21**, 3879-3886 (2021).

3. Peng, Y. et al. Nanoporous polyethylene microfibres for large-scale radiative cooling fabric. *Nat. Sustain.* **1**, 105-112 (2018).

4. Li, J. et al. Protecting ice from melting under sunlight via radiative cooling. *Sci. Adv.* **8**, eabj9756 (2022).

5. Li, D. et al. Scalable and hierarchically designed polymer film as a selective thermal emitter for high-performance all-day radiative cooling. *Nat. Nanotechnol.* **16**, 153-158 (2021).

6. Shi, M. et al. $Ti_3C_2T_x$ MXene-decorated nanoporous polyethylene textile for passive and active personal precision heating. *ACS Nano* **15**, 11396-11405 (2021).

7. Wang, T., Wu, Y., Shi, L., Hu, X., Chen, M. & Wu, L. A structural polymer for highly efficient all-day passive radiative cooling. *Nat. Commun.* **12**, 365 (2021).

8. Li, T. et al. A radiative cooling structural material. *Science* **364**, 760-763 (2019).

9. Li, X. et al. Integration of daytime radiative cooling and solar heating for year-round energy saving in buildings. *Nat. Commun.* **11**, 6101 (2020).

10. Wang, S. et al. Strong, tough, ionic conductive, and freezing-tolerant all-natural hydrogel enabled by cellulose-bentonite coordination interactions. *Nat. Commun.* **13**, 3408 (2022).

11. Wang R, et al. Fabrication of cellulose-graphite foam via ion cross-linking and ambient-drying. *Nano Lett.* **22**, 3931-3938 (2022).

12. Wu, X. et al. An all-weather radiative human body cooling textile. *Nat. Sustain.* (2023).

13. Zhang, Q. et al. Temperature-dependent dual-mode thermal management device with net zero energy for year-round energy saving. *Nat. Commun.* **13**, 4874 (2022).

14. Chen, C. & Hu, L. Nanoscale ion regulation in wood-based structures and their device applications. *Adv. Mater.* **33**, 2002890 (2021).

15. Barthelat, F., Yin, Z. & Buehler, M, J. Structure and mechanics of interfaces in biological materials. *Nat. Rev. Mater.* **1**, 16007 (2016).

16. Wang, Z., Tammela, P., Stromme, M. & Nyholm, L. Cellulose-based supercapacitors: material and performance considerations. *Adv. Energy. Mater.* **7**, 1700130 (2017).

17. Zhang, J. et al. High-barrier, strong, and antibacterial paper fabricated by coating acetylated cellulose and cinnamaldehyde for food packaging. *Cellulose* **28**, 4371-4384 (2021).

18. Li, Y. et al. 2D $Ti_3C_2T_x$ MXenes: Visible Black but Infrared White Materials. *Adv Mater* **33**, 2103054 (2021).

19. Wang, X., Wang, Z. & Qiu, J. Stabilizing MXene by hydration chemistry in aqueous solution. *Angew. Chem. Int. Edit.* **60**, 26587-26591 (2021).

20. Hao, S., Fu, Q., Meng, L., Xu, F. & Yang, J. A biomimetic laminated strategy enabled strain-interference free and durable flexible thermistor electronics. *Nat. Commun.* **13**, 6472 (2022).

21. Wang, Q, W. et al. Multifunctional and water-resistant mxene-decorated polyester textiles with outstanding electromagnetic interference shielding and joule heating performances. *Adv. Funct. Mater.* **29**, 1806819 (2019).

22. Cao, W, T., Ma, C., Mao, D, S., Zhang, J., Ma, M, G. & Chen, F. MXene-reinforced cellulose nanofibril inks for 3D-printed smart fibres and textiles. *Adv. Funct. Mater.* **29**, 1905898 (2019).

23. Li, X., Li, M., Li, X., Fan, X. & Zhi, C. Low infrared emissivity and strong stealth of Ti-based MXenes. *Research* **2022**, 9892628 (2022).

24. Shahzad, F. et al. Electromagnetic interference shielding with 2D transition metal carbides (MXenes). *Science* **353**, 1137-1140 (2016).

25. Rasool, K., Helal, M., Ali, A., Ren, C, E., Gogotsi, Y. & Mahmoud, K, A. Antibacterial Activity of $Ti_3C_2T_X$ MXene. *ACS Nano* **10**, 3674-3684 (2016).